J. Fluid Mech. (2025), *vol*. 1002, A41, doi:10.1017/jfm.2024.1132

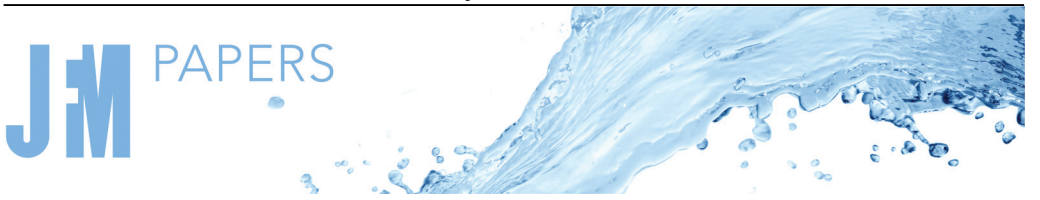

On the interaction between planar incident shock with finite width and cylindrical boundary layer at Mach 2.0

Fangbo Li[1], **Hexia Huang**[1,†], **Huijun Tan**[1], **Xin Li**[1], **Hang Yu**[1] **and Yuan Qin**[1]

[1]College of Energy and Power Engineering, Nanjing University of Aeronautics and Astronautics, Nanjing 210016, PR China

(Received 28 January 2024; revised 11 October 2024; accepted 24 November 2024)

The interaction between planar incident shocks and cylindrical boundary layers is prevalent in missiles equipped with inverted inlets, which typically leads to substantial three-dimensional flow separation and the formation of vortical flow. This study utilizes wind-tunnel experiments and theoretical analysis to elucidate the shock structure, surface topology and pressure distributions induced by a planar shock with finite width impinging on a cylinder wall at Mach 2.0. In the central region, a refraction phenomenon occurs as the transmitted shock bends within the boundary layer, generating a series of compression waves that coalesce into a shock, forming a 'shock triangle' structure. As the incident shock propagates backward along both sides, it gradually evolves into a Mach stem, where the transmitted shock refracts the expansion wave. The incident shock interacts with the boundary layer, resulting in the formation of a highly swept separation region that yields a pair of counter-rotating horseshoe-like vortices above the separation lines. These vortices facilitate the accumulation of low-energy fluid on both sides. Although the interaction of the symmetry plane aligns with free-interaction-theory, the separation shock angle away from the centre significantly deviates from the predicted value owing to the accumulation of low-energy fluids. The primary separation line and pressure distribution jointly exhibit an elliptical similarity on the cylindrical surface. Furthermore, the potential unsteady behaviour is assessed, and the Strouhal number of the low-frequency oscillation is found to be 0.0094, which is insufficient to trigger significant alterations in the flow field structure.

Key words: supersonic flow, shock waves, boundary layer separation

1. Introduction

Shock wave–boundary layer interactions (SWBLIs) are frequently encountered in both internal and external flows of supersonic and hypersonic aircraft, affecting components such as the fuselage, rudder and engine (Green 1970; Herrmann & Koschel 2002).

† Email address for correspondence: huanghexia@nuaa.edu.cn

These interactions induce flow instability and boundary layer separation, which can adversely affect the aircraft performance (Babinsky & Harvey 2011). In external flows, SWBLIs not only affect the lift and drag but also compromise the structural integrity of aerofoil components, posing a significant threat to flight safety (Dolling 2001; Anderson 2010). Specifically, supersonic/hypersonic inlets, which are crucial for the compression components of engines, decelerate and pressurize high-speed inflow through a series of shock waves (Huang *et al.* 2023). When SWBLIs occur in the internal flow of the inlet, they give rise to various types of separated flows, negatively affecting internal flow quality by reducing inlet efficiency, increasing flow distortion, and potentially causing unstart, which could lead to catastrophic flight failure (Délery 1985; Babinsky & Ogawa 2008; Krishnan, Sandham & Steelant 2009; Chang *et al.* 2017; Huang *et al.* 2018).

Since the pioneering discovery of the SWBLI phenomenon by Ferri (1940), there has been considerable researches devoted to various SWBLI configurations (Fage & Sargent 1947; Barry, Shapiro & Neumann 1951; Liepmann, Roshko & Dhawan 1952). In recent decades, the complex flow structure and internal mechanisms governing these interactions have been progressively elucidated from theoretical and experimental perspectives, particularly in the context of transonic and supersonic speed regimes (Délery & Marvin 1986). Certain SWBLIs exhibit distinctive quasi-two-dimensional properties (Dolling 2001; Babinsky & Harvey 2011), notably including incident SWBLIs (ISWBLIs) and compression ramp SWBLIs, further revealed by detailed investigations into their flow field structures and foundational mechanisms (Green 1970; Ramesh & Tannehill 2004; Dupont, Haddad & Debiève 2006; Souverein, Bakker & Dupont 2013; Sriram *et al.* 2016; Zhu *et al.* 2017; Volpiani, Bernardini & Larsson 2018; Li *et al.* 2022, 2023). In practical applications, however, the unique geometric configurations of aircraft often lead to spanwise non-uniformities in shock waves and boundary layer characteristics, resulting in prominent three-dimensional SWBLIs. Such three-dimensional interactions include those induced by protuberances (Bhardwaj, Hemanth Chandra Vamsi & Sriram 2022; Nimura *et al.* 2023), sharp fins (Gaitonde & Knight 1991), double cones (Wright *et al.* 2000; Nompelis, Candler & Holden 2003), cylinder shocks (Combs *et al.* 2018; Lindörfer *et al.* 2020), ogive–cylinder/inclined flares (Garcia *et al.* 2018) and axial wedge corner flows (Sabnis & Babinsky 2023). These three-dimensional SWBLIs engender unique phenomena and distinctive similarity attributes, which have been comprehensively characterized and reviewed by Délery (1993). The complex three-dimensional shock-induced separated flows associated with protuberances reveal a sophisticated horseshoe vortex structure (Voitenko, Zubkov & Panov 1966; Sedney 1973). Moreover, the notion of 'quasiconical similarity' (Kubota & Stollery 1982; Settles & Lu 1985; Settles & Kimmel 1986) has been validated in SWBLIs generated by sharp fins, semi-cones and swept compression corners (Panaras 1996; Gaitonde 2015), as evidenced through oil-flow visualization techniques (Sheng *et al.* 2018) and spectral analysis of wall pressure fluctuations (Schmisseur & Dolling 1994).

Moreover, it is evident that not only does the shock wave contribute to significant three-dimensional effects in SWBLIs, but the boundary layer itself also plays a significant role in this phenomenon. Among the various three-dimensional SWBLI configurations, a distinctive type emerges, characterized by a conical shock or cylindrical boundary layer that possesses a constant curvature that resembles that of a flat plate. The constant curvature yields a distinctive pressure gradient in the spanwise direction, resulting in considerable lateral flow in the separation region. The fin-on-cylinder SWBLIs markedly departs from the quasiconical symmetry typically observed in planar fin SWBLIs, illustrating the distinctive upheaval of the three-dimensional curved boundary layer

(Pickles *et al.* 2019). Previous investigations (Panov 1971) focusing on the interaction between conical shocks and two-dimensional boundary layers have provided valuable insights into the flow field characteristics under both separated and attached conditions. Notably, significant lateral flow phenomenon has been documented, attributed to considerable pressure gradients in the spanwise direction, manifesting in the formation of a horseshoe vortex in the separation region, which gradually diminishes in strength away from the symmetry plane (Gai & Teh 2000; Zuo *et al.* 2019). Experimental investigations involving SWBLIs with conical configurations both inside and outside a cylindrical body have corroborated the existence of the horseshoe vortex (Kussoy, Viegas & Horstman 1980). Several distinct experimental studies conducted independently by Morkovin *et al.* (1952) and Brosh, Kussoy & Hung (1985), examined a planar shock impinging obliquely on a cylinder, revealing remarkable boundary-layer cross-flow and wake-type flow characterized by double separation induced by sharp pressure gradients. In addition to identifying analogous horseshoe vortex formations, numerous experiments (Stephen *et al.* 2013; Robertson *et al.* 2015; Mason, Natarajan & Kumar 2021) utilizing oil flow visualization, schlieren photography, pressure-sensitive paint technique, particle image velocimetry (PIV) and unsteady pressure measurement have elucidated significant variations in lateral force and pitching moment characteristics of the cylinder. These variations are primarily attributed to substantial pressure fluctuations occurring beneath the shock foot and in the regions of flow reattachment. The PIV results further indicate that intense separation flow on the body generates a highly unsteady closed bubble characterized by pronounced periodic reversed flow, while weak separation manifests as an open-type region (Kiriakos *et al.* 2022).

Furthermore, the interaction between planar shock waves and curved boundary layers has significant relevance in various engineering applications. A pertinent example is the German antiradiation missile, designated as the 'Aemiger', which features a configuration of four inverted two-dimensional inlets arranged in an X-shaped layout around the projectile body. The planar shock, characterized by a finite width and generated at the compression surface of the two-dimensional inlets, interacts with the curved boundary layer of the projectile body. Due to the confinement effect, the dynamics of the interaction between the planar incident shock and boundary layer with finite width exhibit distinct characteristics, compared with interactions involving an infinite width boundary layer. In this study, a set of simplified experimental test models was developed, incorporating an ogive–cylinder geometry alongside a planar shock generator with a relatively narrow width, reflective of the inverted inlet configuration mounted in the missile design. A series of measurement techniques was utilized in experimental investigations to elucidate the time-averaged structure of planar shock–cylindrical boundary layer interactions (PISCBLIs) in proximity to the wall. Additionally, computational fluid dynamics (CFD) methods were performed to further complement the experimental findings, with the objective of clarifying the three-dimensional characteristics and underlying flow mechanisms governing by PISCBLIs.

2. Experimental set-up and numerical methods

2.1. *Introduction of the test model*

To simplify the inlet/projectile model, a cone body with a half-angle of 8° was assembled in front of the ϕ 100 mm diameter cylinder, as depicted in figure 1(*a*). The planar shock generator, with a finite width of 60 mm, was positioned directly above the cylinder, equipped with two lateral side plates to preserve the planar configuration of

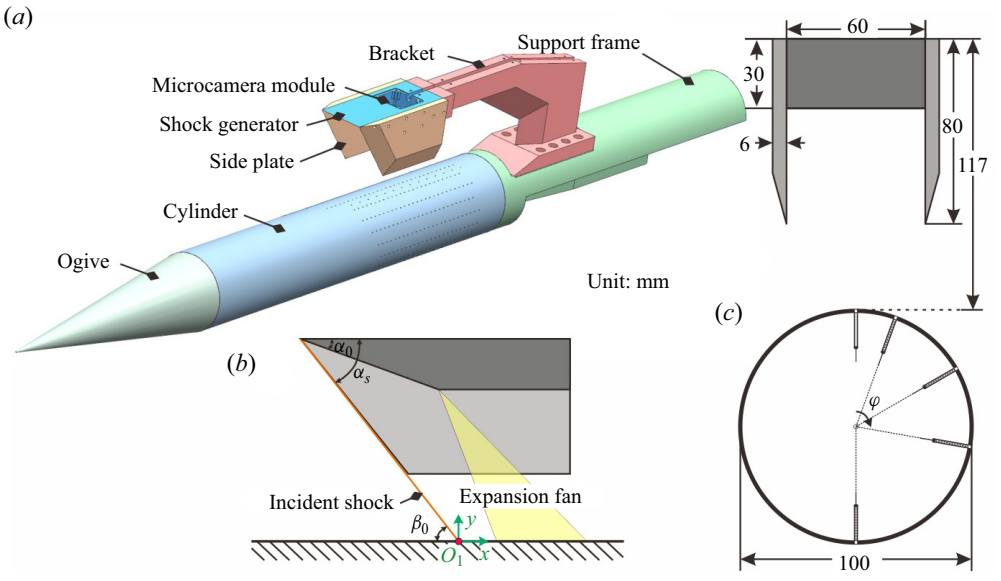

Figure 1. Experimental set-up of the test model: (*a*) schematic diagram of parts assembly; (*b*) configuration of the shock generator; (*c*) spanwise dimensions of the test model.

the shock wave. Situated 255 mm downstream of the conical expansion fan emanating from the shoulder, the shock generator ensured a uniform and undisturbed incoming flow. Figure 1(*b*) provides a schematic diagram of the shock generator along with its side plates. To mitigate the impact of the tailing expansion fan on the interaction between the incident shock and boundary layer, the initial compression surface of the shock generator was designed to be extended to the maximum feasible length. The angle of the shock generator, denoted as α_0, was set at 15°, which resulted in a corresponding shock angle β_0 of 45.34° at an incoming Mach number of 2.0. The two side plates flanking the shock generator ensured the integrity of the planar shock, with the leading-edge sweep angle α_s being 0.5° smaller than the shock deflection angle, as is consistent with sidewall inlet designs. The point of the shock impinging on the symmetry plane, labelled as O_1, served as the reference coordinate origin for schlieren imaging and oil-flow pattern analysis in subsequent investigation. Figure 1(*c*) illustrates the relative positioning of the generator with respect to the cylinder in the z–y cross-section, oriented perpendicular to the flow direction. Key dimensional parameters, including the width and height of the shock generator (60 and 117 mm, respectively), are distinctly defined.

Meanwhile, the positive direction of the circumferential angle φ is defined as clockwise when viewed from the perspective of the incoming flow, with the upper centreline aligned at 0° within the range of 0°–180°. Static pressure tappings were arranged on the surface of the cylinder at various circumferential positions (0°, 20°, 60°, 100° and 180°) within this range. Five rows of pressure tappings, each with a diameter of 1.0 mm, were arranged in a streamwise orientation, with an 8 mm spacing between adjacent tappings located at the same circumferential position. The initial pressure tapping was positioned approximately 100 mm upstream on the shock-impinging point. Furthermore, a microcamera module installed inside the shock generator and connected to a support frame in the wind tunnel recorded real-time oil-flow patterns on the cylinder wall. For clarity in subsequent analysis

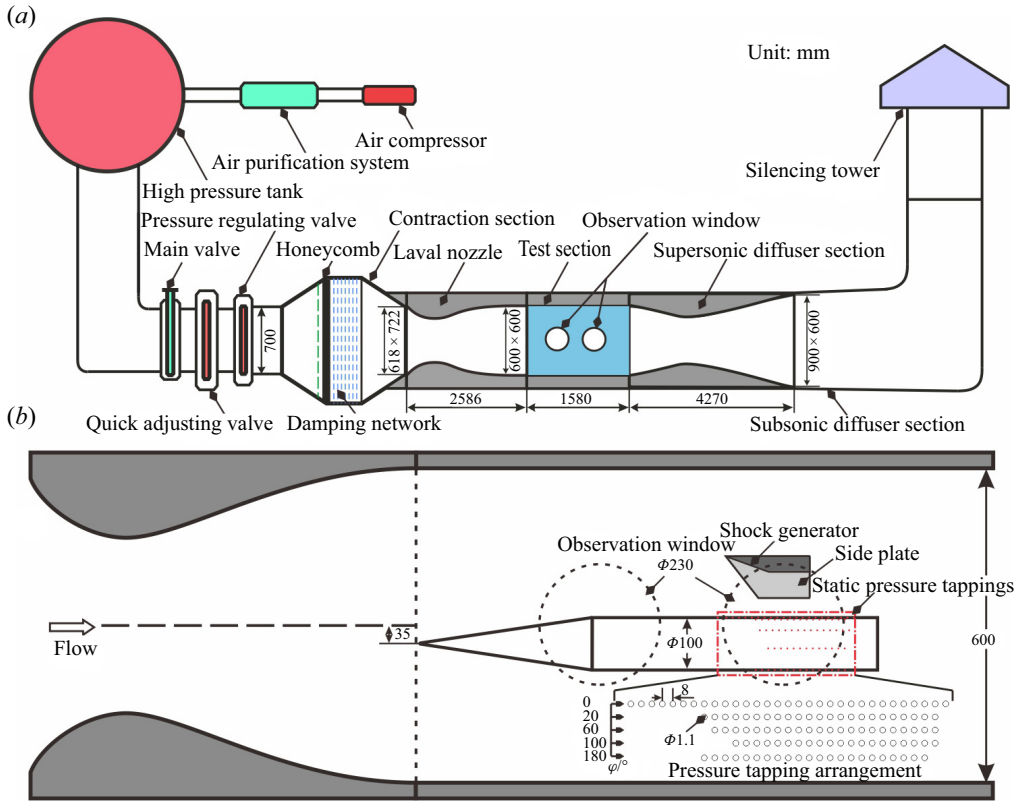

Figure 2. Set-up of the wind tunnel: (*a*) schematic diagram of the NH-1 wind tunnel; (*b*) relative position of the test model in the wind tunnel.

and discussion, the streamwise, transverse and spanwise directions of the test model are designated as the x-, y- and z-axis, respectively (figure 1).

2.2. *Wind tunnel and measurement methods*

All experiments were conducted in the NH-1 transonic wind tunnel at Nanjing University of Aeronautics and Astronautics, which is a direct-connect facility fed by an upstream high-pressure source and utilizing a downstream atmospheric environment. As illustrated in figure 2(*a*), high-pressure gas is compressed by an air compressor and stored in the tank. The NH-1 wind tunnel is capable of operating with a nominal Mach number ranging from 0.2 to 4.0, allowing for steady operation duration exceeding 40 s during each test. The dimensions of the test section measure 600 mm × 600 mm in width and height, and it features two pairs of optical glass windows, each with a diameter of 230 mm, positioned at the central height on both sides. In this study, the nominal Mach number of the incoming flow is set at 2.0, with an actual incoming Mach number of 1.98. The total pressure and temperature of the incoming flow are 188 kPa and 282 K, respectively.

Figure 2(*b*) depicts the relative positioning of the model within the test section. The interaction region is located in the middle of the second observation window, with the centre of the cylinder situated 35 mm below the centre of the test section. Figure 3 provides assembly drawings of the test model installed in the wind tunnel, where the apex of

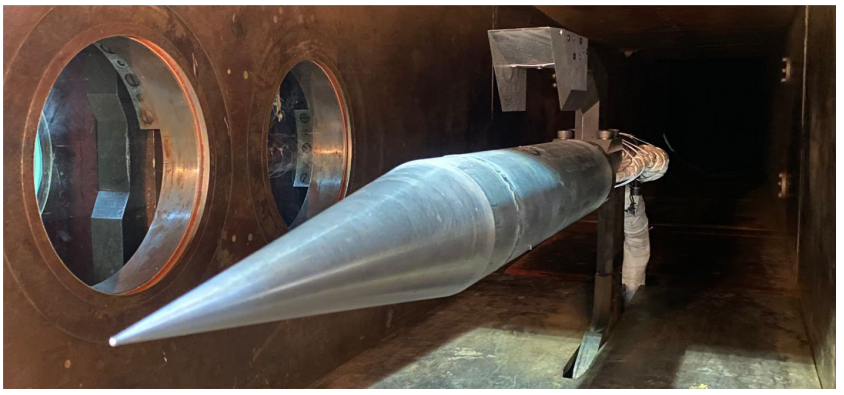

Figure 3. Photographs of the test model installed in the test section of the wind tunnel.

the cone features a rounded profile with a diameter of 1.5 mm. To force the boundary layer transits to a fully turbulent state, a serrated leading-edge boundary layer strip was circumferentially affixed posterior to the shoulder expansion fan.

Pressure measurements were conducted using the ESP-64 HD pressure scanner system by MEAS Inc., which is capable of operating within a range of 15 p.s.i. and achieves an accuracy of 0.03 % full scale. To evaluate the velocity distribution of the undisturbed turbulent boundary layer, a Pitot pressure measuring system was strategically positioned 100 mm upstream of the shock impinging point O_1 (as indicated in figure 1). The microPitot tube, affixed to the moving support plate actuated by a linear-stepping motor, has a length of 15 mm, with its leading edge situated 1 mm downstream of the static pressure measuring point. Notably, the entire Pitot tube system is installed along the internal wall of the cylinder to eliminate potential interference with the experimental model. Moreover, pressure sensors with a diameter of 3.5 mm, a range of 100 kPa, and an accuracy of 0.1 % full scale are employed to capture transient pressure signals on the wall surface. Previous study (Clemens & Narayanaswamy 2014) have established that the low-frequency oscillation frequency associated with large-scale separation bubbles typically does not exceed 1 kHz. In this study, the pressure sensor operates at a sampling frequency of 20 kHz.

To achieve precise visualization of the flow structure within the interaction region, a 'Z'-type schlieren system was utilized in this experiment. Schlieren images were captured using a Canon 1Dx Mark II camera, equipped with a Nikon AF vr80-400 mm F/4.5–5.6D zoom lens. During the testing phase, the shutter speed was set to 1/8000 s and the ISO was adjusted to 200 to maximize incoming light and enhance sensitivity. A horizontal knife edge was utilized to facilitate detailed observation of the flow field structure in the interaction region. Concurrently, the flow field adjacent to the cylinder was visualized using the oil-flow method. Prior to the tests, a mixture of silicone oil, oleic acid and titanium dioxide powder was uniformly applied to the surface of the blackened cylinder model. To capture real-time videos of the oil-flow patterns on the cylinder during wind tunnel operation, an microcamera module was installed within the shock generator, alongside an external camera positioned near the observation window. Furthermore, two 100 W light emitting diode lamps are mounted at the first observation windows on both sides to illuminate the cylinder wall effectively.

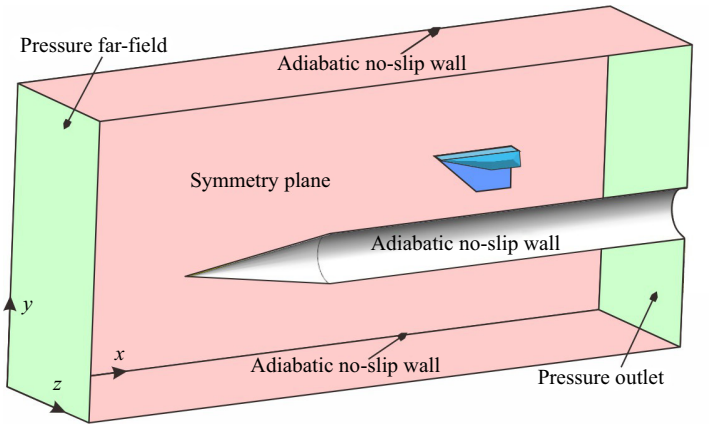

Figure 4. Set-up of the computational domain (the symmetry plane shows transparency).

2.3. *Numerical simulation methods*

The three-dimensional compressible Reynolds-averaged Navier–Stokes equations were solved by the finite volume method. The turbulence flow was modelled utilizing the SST k–ω model, regarding the air as an ideal gas. The Sutherland formula was applied to determine the viscosity coefficient of the airflow. An implicit time-marching method was employed to enhance convergence, while a second-order upwind scheme was applied for the discretization of the governing equations of the flow field. Flow parameters, including the mass flow rate and mass-weighted-average Mach number at the outlet plane, were monitored throughout the computation. The calculation was deemed sufficiently converged when each monitoring parameter remained stable, with residual falling below an order of magnitude 10^{-4}. Detail of the validation of the CFD methods are provided in the Appendix, eliminating the need for further elaboration here.

The parameters of the incoming flow in the numerical simulation align with those obtained in the experiment set-up, and the scale of the computational domain and the relative position of the model also correspond directly to the experimental conditions. To enhance computational efficiency and conserve resources, half of the test models were selected for analysis. As shown in figure 4, the inlet and outlet boundaries are specified as pressure far-field and pressure outlet conditions, respectively. The sides of the computational domain are configured as adiabatic no-slip walls, simulating the upper and lower boundaries of the wind tunnel. The computational domain is discretized using a hexahedral structured grid consisting of 16×10^6 cells. The height of the first layer of grids is 0.0056 mm according to $y^+ = y_1 u_\tau / \upsilon$ (Fang *et al.* 2020), with a growth rate 1.1 following a parabolic (bigeometric) relation from the wall to the free stream. The tip of leading-edge cone was subjected to rounding treatment with a radius of 0.2 mm to avoid local erosion. An 'O-grid' structured mesh was used to divide the rounded shape of the leading-edge cone. Adaptive mesh refinement techniques were applied based on the pressure gradients, with local refinement applied to the grids adjacent to both the planar and conical shocks, thereby enabling accurate capture of the shock structures and three-dimensional vortex topology, resulting in a finely resolved flow field.

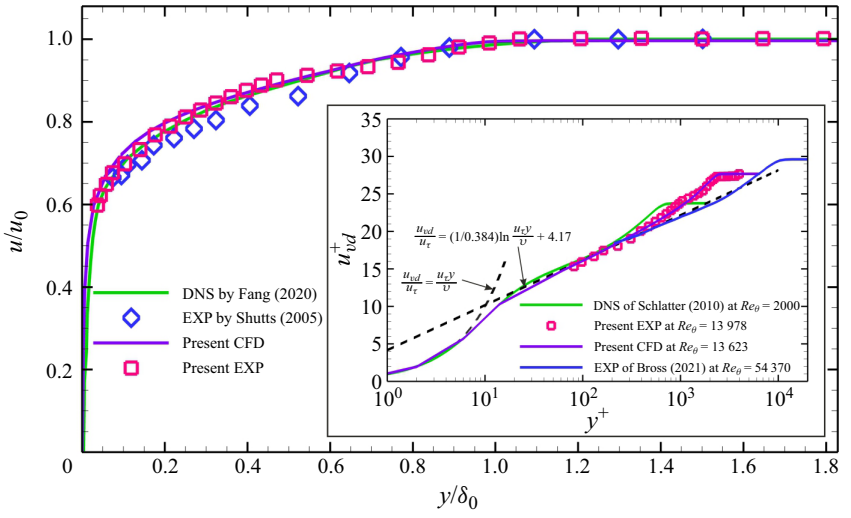

Figure 5. Velocity profile of the incoming boundary layer.

3. Results

3.1. *Upstream incoming turbulent boundary layer*

Initially, the flow parameters of the boundary layer were measured at a location 255 mm downstream of the leading edge of the cylinder (slightly upstream of the interaction region) using a Pitot tube system, with the shock generator removed. As the Pitot tube traversed vertically via a motorized mechanism, it was assumed that the static pressure along the radial direction holds invariant, equal to the pressure value in front of the Pitot probe on the cylinder wall. Employing the Rayleigh–Pitot pressure relation (Anderson 2010), the measured Pitot pressure profile and static pressure are converted to obtain the Mach number profile of the boundary layer. The radial height corresponding to 0.99 times the mainstream velocity u_0 was designated as the boundary layer thickness δ_0. The u_0 and δ_0 served as the velocity and length scale references for normalization, thereby yielding the standard boundary layer velocity profile. The Pitot tube system was removed for subsequent tests after measurement to eliminate its effect on the downstream flow. In order to ensure the fidelity and accuracy of the numerical simulation, the numerical boundary layer profiles were also extracted in figure 5 to verify the consistency between the numerical simulation and experimental data. Both the outcomes from direct numerical simulation (DNS) by Fang *et al.* (2020) and experiments by Shutts, Hartwig & Weiler (1955) demonstrated a congruent distribution of boundary layer velocity profiles with those of the present study, indicating that the boundary layer examined in this paper is an undisturbed fully turbulent boundary layer.

Based on the velocity profile described above, the boundary layer parameters from both the numerical simulation and experimental measurements were converted by the van Driest transformation (van Driest 1951). The method of estimating wall friction proposed by Kendall & Koochesfahani (2008) is employed to calculate the friction velocity u_τ at the cylinder wall. The converted u^+ is substituted with u^+_{vd} to account for compressible effects, which are related to velocity and temperature. Note that the wall is considered nearly adiabatic throughout this process. As illustrated in figure 5, the transformed velocity profile exhibits a strong correlation with the logarithmic law within a

Ma_0	u_0 (m s^{-1})	δ_0 (mm)	δ^* (mm)	θ (mm)	H (mm)	Re_θ	$C_{f,0}$
1.98	492	6.82	0.82(1.49^a)	0.64(0.53^a)	1.28(2.80^a)	16 908(13 978^a)	0.00173

Table 1. Parameters of the turbulent boundary layer.

specific range, as proposed by Monkewitz & Nagib (2023) for typical turbulent boundary layers.

In accordance with the Busemann relation (White & Majdalani 2006) and the adiabatic wall condition, and assuming a turbulence recovery coefficient $r = 0.89$, the temperature and density distributions in the boundary layer were calculated. Subsequently, the momentum thickness and the shape factor of the boundary layer were determined through the integral formula. The Reynolds number based on the momentum thickness was then derived. Utilizing the previously established relation $C_f = 2\rho_\omega u_\tau^2/\rho_0 u_0^2$, the wall friction coefficient in the experiment C_f determined from the experimental data was found to be 0.00173, where ρ_ω represents the density of fluid in the vicinity of the wall. Given that the log law of the cylindrical boundary layer appears substantially identical to that of a planar boundary layer with von Kármán's constant, $\kappa = 0.4$, particularly when the transverse curvature is negligible ($\delta_0/0.5D \ll 1$) (Lueptow 1990; Kumar & Mahesh 2018), the mean velocity profile of the cylindrical boundary layer at the same streamwise location can be considered precisely duplicate. Table 1 lists the relevant parameters of the undisturbed turbulent boundary layer in the experiments, with the superscript ^{a} indicating the compressible amount derived from the density distribution.

3.2. *Shock structure within the central region*

The flow field structure was observed through the time-resolved schlieren image captured by a camera. By using a horizontal knife edge, the image depicts the differential density variations in the vertical direction. Additionally, numerical schlieren results are calculated to reveal the density gradient of the fluid along the y-direction, thereby highlighting the vertical gradients within the flow field. Figure 6 presents a comparison of the flow structure on the symmetry plane between the experimental and CFD results, with the origin of the coordinates set at the impinging point O_1 of the incident shock. While the schlieren images in the experiment showed slight oscillations attributable to integration effects and camera shake, the underlying flow field structure remains unaffected, manifesting primarily as variations in image brightness. Figure 6(a) presents an averaged result derived from multiple clear snapshots, which unveils the characteristic flow field structure associated with steady flow. Akin to ISWBLIs on a flat plate, the incident shock (i) induces a prominent 'separation bubble' near the cylinder wall. A regular reflection occurred above the separation, giving rise to a separation shock (s_1) and two transmission shocks (ts_1, ts_2). Both the experimental and numerical schlieren visualizations show an oblique shock emerging downstream of the intersection point of the incident shock and separation shock, thereby forming a closed 'shock triangle' structure. It is noteworthy that the 'shock triangle' structure and the separation region are interconnected by a shock that gradually transitions to a Mach stem at the bottom of the boundary layer.

Figure 7 illustrates the flow structure diagram corresponding to the schlieren images previously described. Within the central region of PISCBLIs, a separation flow exhibiting an approximately triangular configuration is induced adjacent to the cylinder wall. This is distinctly manifested as a two-dimensional closed separation 'bubble' formed between

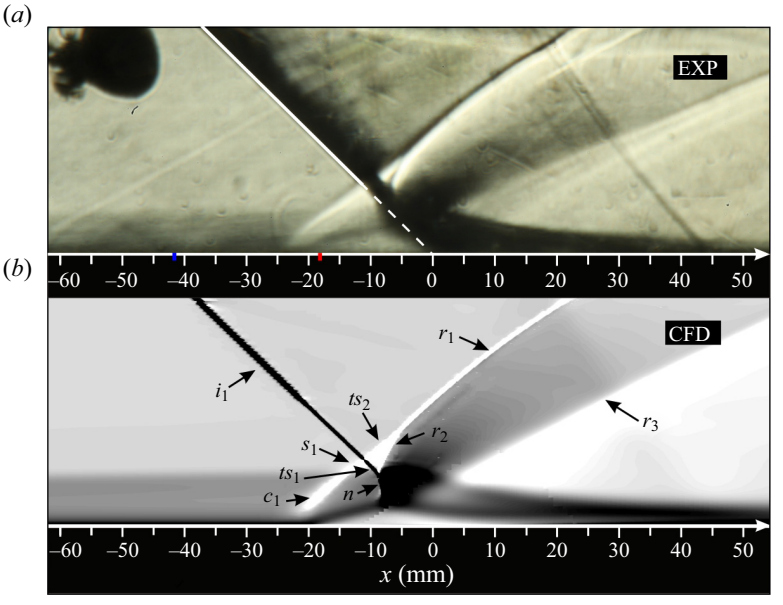

Figure 6. Schlieren photographs of the experimental and numerical flow field structure: (*a*) experimental results; (*b*) numerical results (i_1, incident shock; s_1, separation shock; ts_1, ts_2, transmitted shock; r_1, reflected shock; r_1, refraction shock; r_3, reattachment shock; c_1, compression wave. The blue and red short lines represent the dynamic pressure measurement positions upstream and downstream of the separation point on the centreline, respectively).

the saddle point S, the node point R and the separation streamline (Q). As the incident shock traverses the intersection point, it generates a transmitted shock ts_1 (C_4). Due to the significant velocity gradient within the incoming boundary layer, the transmitted shock experiences continuous bending, transforming from an oblique shock to a Mach stem (C_6) above the separation bubble. Notably, the elevation of the sound speed line in the local region in front of the Mach stem is a critical feature. The transmitted shock C_4 reflects a series of compression waves in the upper region of the boundary layer, which converges downstream into the reflected shock (C_5) and intersects with another transmitted shock ts_1. Collectively, transmitted shocks ts_1, ts_2 (C_3, C_4), and reflected shock (C_5) create a 'shock triangle' structure, with the underlying formation mechanisms to be elaborated upon in subsequent discussions. Downstream of the Mach stem, the aerodynamic surface resulting from the separation bubble establishes a divergent channel, facilitating the emergence of an expansion wave region above the separation bubble. Additionally, this expansion wave compels the transmitted shock (C_3) to undergo a certain degree of bending. The airflow downstream of the expansion waves collides with the wall, leading to the formation of a series of compression waves that ultimately converge to form a reattachment shock.

To enhance the understanding of the inviscid flow structure within the central region, a shock polar analysis is utilized. As shown in figure 8, the separation shock is determined by the undisturbed boundary layer in accordance with the turbulent separation criterion (Grossman & Bruce 2018). For the separation induced by the incident shock in the symmetry plane, the shock angle β_2 and flow deflection angle α_2 (deflected away from the wall) of the separation shock s_1 are fixed at 39.84° and 10.11°, respectively, with a Mach number of 1.62 behind it. Owing to the relatively low intensity of the incident shock (C_1), the resultant Mach number downstream of the wave is relatively high, resulting in the shock polar (Γ_1) intersecting with the separation shock (Γ_2). The intersection of Γ_1 and Γ_2

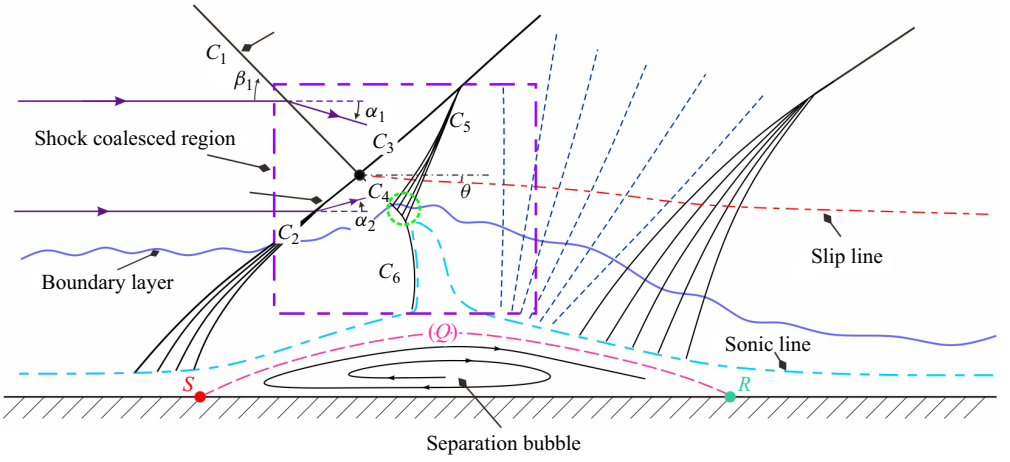

Figure 7. Schematic diagram of flow structure of the shock-induced separation within the central region. Here C_1–C_6 are the expressions of several shock waves in the shock polar. Here $0 < z/D < 0.3$, regular reflection (RR)

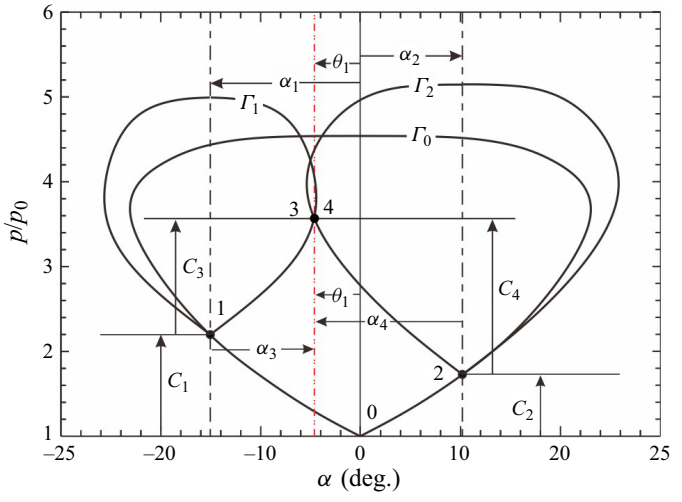

Figure 8. Shock-polar representation of the regular interaction structure.

delineates two states (3, 4) across the slip line, signifying two distinct airflow streams with equal pressure but different velocities, as described by the Rankine–Hugoniot equations. The deflection angles between both streams are computed to be $\theta = -4.33^\circ$.

The unique refraction phenomenon of the shock (Henderson 1967) within the boundary layer are elucidated, providing a fundamental explanation for the formation of the 'shock triangle' structure. As depicted in figure 9, viscous effects are neglected, and the separation bubble is modelled as a bulged aerodynamic surface. This approximation permits the continuous Mach number distribution within the boundary layer to be substituted with an incremental profile composed of numerous thin parallel streams of inviscid gas (Henderson 1966, 1967). When the transmitted shock ts_1 encounters the outer edge of the boundary layer with an idealized velocity distribution, it is refracted by the first incremental change in the Mach number (M_{20}–M_{21}), bending into t_1, accompanied by the simultaneous appearance of compression wave r_1. Subsequently, as t_1 progresses

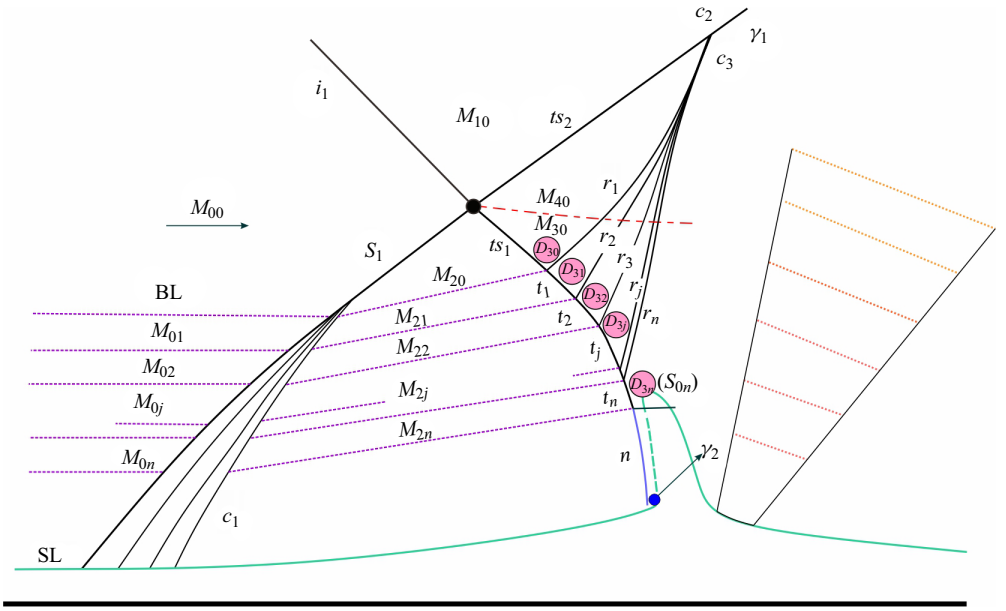

Figure 9. Refraction of the shock in the shock coalesced region (in the symmetry plane): t_1, t_2, t_j, t_n, the refraction of transmitted shock in the boundary layer; r_1, r_2, r_j, r_n, the refraction of transmitted shock in the boundary layer; D_{30}, D_{31}, D_{32}, D_{3j}, D_{3n}, the airflow parameters behind shock ts_1, t_1, t_2, t_j, t_n; sl_1, sl_2, slip line; boundary layer BL; sonic line SL. Here $z/D = 0$, regular reflection (RR).

downward through the boundary layer, it leans towards the vertical direction, transforming into $t_2 \ldots t_j \ldots t_n$, behind which a series of compression waves ($r_2 \ldots r_j \ldots r_n$) are generated and converge above to form a shock c_3, which intersects with the transmitted shock of the separation shock ts_2. As the airflow of M_{2n} traverses shock t_n, it reaches sonic conditions, denoted as S_{on}, at which point the refracted compression waves cease. Below shock n, a normal shock is established, characterized by varying curvature related to the deflection angle and velocity gradient of the airflow in front of the normal shock n. A local subsonic airflow region appears behind the normal shock, leading to a significant decrease in the height of the separation bubble. This forms an aerodynamic contraction channel, resulting in the appearance of expansion waves that quickly reaccelerate the local airflow from subsonic to supersonic.

The generation mechanism of compression waves (r_1,$r_2 \ldots r_j \ldots r_n$) can be analysed through the shock polar in figure 10. After traversing through the incident shock i_1 and the separation shock s_1, respectively, the incoming flow at Mach number M_{00} (D_0) transitions to airflow characterized by Mach numbers M_{10} (D_1) and M_{20} (D_2), respectively. As the airflow streams (M_{10}, M_{20}) pass through transmitted shocks ts_1 and ts_2, the deflection angle and pressure of the airflow (M_{30}, M_{40}) converge, forming point D_3 ($p_{30}/p_{00} = 3.67$, $\alpha_{30} = -4.33^\circ$) in the shock-polar diagram. As shown in figure 10, the shock polar shifts downward as the Mach number decreases. From state D_{30} to state D_{3j}, the Mach number declines from $M_{20} = 1.62$ to $M_{2j} = 1.41$, with the intersection points of polar curves at various Mach numbers maintaining proximity to the origin point D_2. Consequently, in the local region where the airflow deflection angle gradually decreases from $\alpha_{20} = -14.44^\circ$ ($\alpha_{20} = \theta - \alpha_{10} = -4.33^\circ - 10.11^\circ = 14.44^\circ$) to zero and subsequently ascends, the shock polar associated with lower Mach numbers is always located inside the higher Mach number polar curve. When the Mach number is below 1.41 (corresponding to the

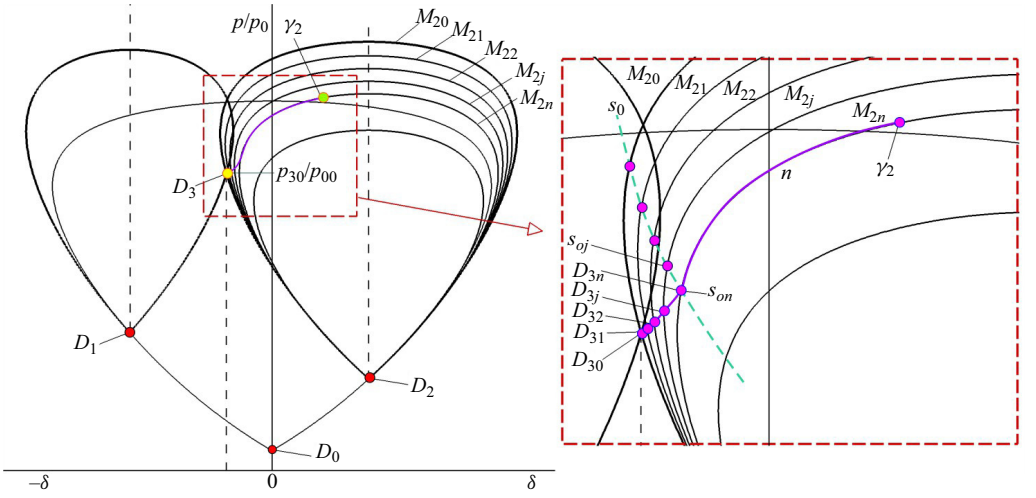

Figure 10. The expression of shock refraction in the shock-polar diagram (in the symmetry plane).

D_{3j} state), apart from the origin point D_2, wherein the shock polars of low Mach numbers are completely located inside those of high Mach numbers.

Upon entering the boundary layer, the reduction in Mach number (M_{20}–M_{21}) leads to an increase in the angle of shock t_1 and the airflow deflection angle following shock t_1, as compared with the incident shock i_1. A compression wave is necessary to raise the pressure and facilitate the transition from state D_{30} to D_{31}. By an analogy, the shock incessantly refracts towards a direction as it further penetrates the boundary layer from t_1 to t_j until t_n, causing the deflection angle of the airflow to decrease and the pressure behind the shock to rise from state D_{31} to D_{3n} continuously. Consequently, a series of compression waves with varying directions are generated, coalescing into an oblique shock located above the refraction region. The airflow behind shock t_n has reached sonic condition, corresponding to the intersection (S_{on}) of M_{2n} and the sonic speed line S_0 in the shock-polar diagram. The transmitted shock ultimately terminates above the separation bubble as a normal shock n. Furthermore, the airflow behind the strong shock n is subsonic flow, expressed as a curved line n between point S_{on} and γ_2 in the shock-polar diagram.

3.3. *Three-dimensional effect of the PISCBLIs flow field*

Considering the distinctive three-dimensional effects induced by the curved boundary layer in PISCBLIs, a qualitative analysis was conducted to elucidate the shock structure derived from the spatial flow field, depicted in figure 11. The reversed flow region, highlighted in pink, exhibits a short and broad curved profile, with its spanwise width slightly increasing in the downstream direction. Notably, the reversed flow region initially curves downward and subsequently upward in the vertical direction, forming a miniature bump along the streamwise direction. A prominent feature is the presence of a minor depression distributed along the spanwise direction within the separation bubble, where a portion of the airflow deflects laterally on both sides. In the central region ($0 \leq z/D < 0.3$), the angle and streamwise position of the incident shock remain almost invariant. As a result, the ‘shock triangle’ structure and the separation region exhibit consistent shapes along the spanwise direction. However, owing to the swept-back nature of the separation bubble, the position of the compression shock shifts downstream along the

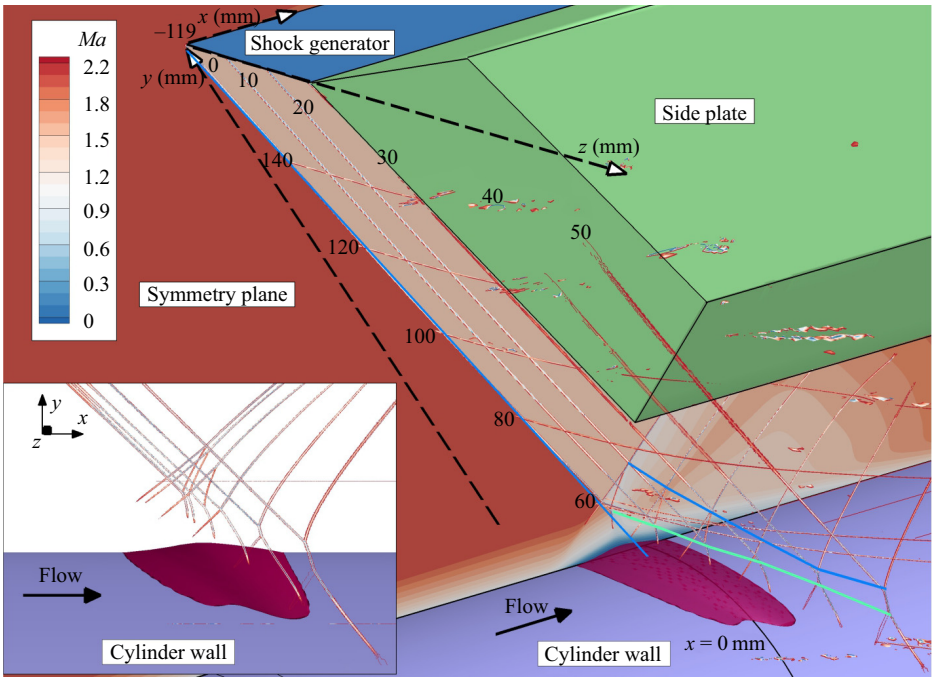

Figure 11. The distribution of the spanwise flow structure and separation near the cylinder wall.

spanwise direction, resulting in a backward motion of the shock intersection point. Additionally, the height of shock intersection points diminishes along the spanwise direction due to the downward bending of the wall, leading to a reduction in the size of the 'shock triangle' structure. However, in the outer region ($z/D > 0.3$), the ramp shock sweeps backward along the spanwise direction, substituting the incident shock interaction with a swept shock interaction. The curved swept-back shock interacts with the curved boundary layer, leading to the formation of a Mach stem structure, without reversed flow emerging in this region.

The flow field structures represented in six spanwise slices, as depicted in figure 11, are extracted and illustrated in figure 12, where the $z/D = 0$ section represents the symmetry plane, with the other sections being parallel to it. Within a specific range of $0 < z/D < 0.3$, there is a descending scale of the 'shock triangle' structure in the flow field. Upon reaching the edge of the shock generator width at $z/D = 0.3$, the 'shock triangle' structure dissipates and is supplanted by a typical four-shock intersection configuration. For spanwise distances exceeding the shock generator width ($z/D > 0.3$), an inclined Mach stem appears in the flow field (figure 12*e*,*f*), which continuously increases in height with the increase in spanwise distance z/D. As illustrated in figure 13, the state of the airflow behind the intersection of the incident and separation shock on the symmetry plane ($z/D = 0$) is represented as D_{30}, necessitating a compression wave to counterbalance downstream pressure. As the spanwise distance increases, fluid within the central separation region diverts and accumulates laterally, resulting in a continuous increase in the height of the local separation bubble. Consequently, the separation shock intensifies, leading to a substantial increase in the airflow deflection angles. Behind the separation shock, the airflow parameter D_2 moves along the shock polar of D_0 in the direction of a growing deflection angle. The intersection point between the separated shock wave and the incident shock wave gradually shifts from $D_{30,a}$ to $D_{30,d}$, eventually leading

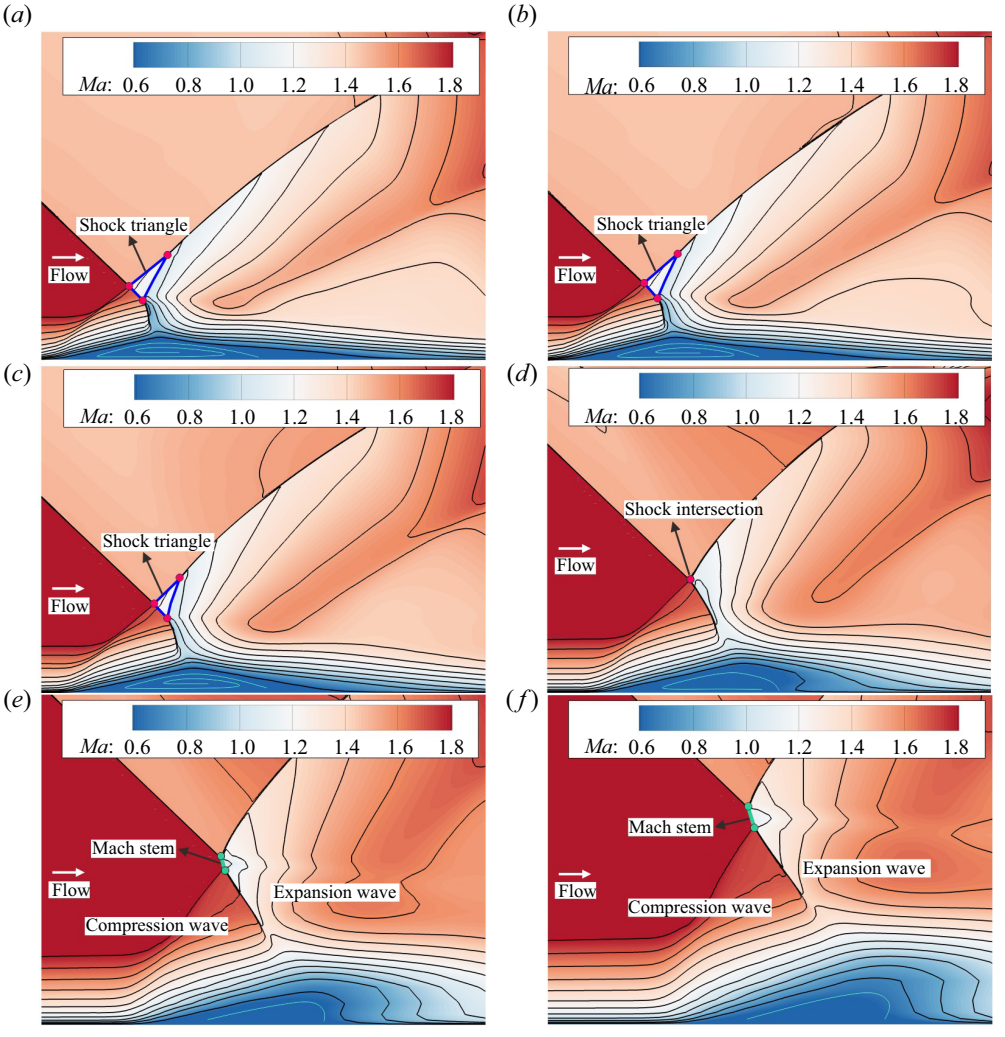

Figure 12. Flow field structure at different cross-sections along the spanwise direction: (*a*) $z/D = 0$; (*b*) $z/D = 0.1$; (*c*) $z/D = 0.2$; (*d*) $z/D = 0.3$; (*e*) $z/D = 0.4$; (*f*) $z/D = 0.45$.

to the complete disappearance of the refracted compression wave, corresponding to two polar curves that no longer intersect.

The shock refraction phenomenon and the formation of the 'shock triangle' structure cease beyond two side plates. At this point, a Mach stem emerges between the incident shock and separation shock, which continuously increases in height along the spanwise direction. Moreover, the accumulation of low-energy fluids on both sides significantly results in a significant thickening of the boundary layer. However, there is no discernible reversed flow, and the airflow within the boundary layer no longer reverses but instead deflects towards the cylinder wall. Simultaneously, the separation shock dissipates and is replaced by a series of compression waves, which increases the Mach number behind them when compared with the region behind the separation. Furthermore, the airflow parameters located downstream of the compression wave can be simplified as points on the isentropic polar line in the shock-polar diagram. As shown in figure 13, the curve *n* between

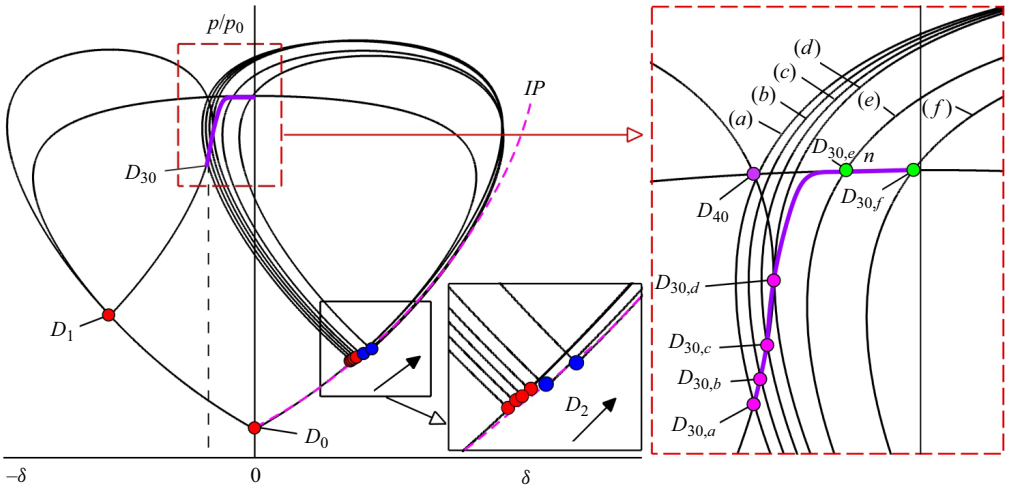

Figure 13. Schematic diagram of shock-polar at different spanwise positions; isentropic polar (*IP*)

points $D_{30,e/f}$ and D_{40} represents the Mach stem, which inclines to a certain degree due to different pressure rises at varied deflection angles. As the angle of the compression wave increases, the deflection angle of the downstream airflow ascends, causing the shock polar emanating from point D_2 to shift to the upper right-hand side. Consequently, the height of the Mach stem accordingly increases as the point D_{30} shifts to the right-hand side.

By analysing the flow fields on the inner and outer sides of the side plate, one can observe a clear transition from a 'shock triangle' structure to a Mach stem configuration, along with notable discrepancies in the shock refraction phenomenon within the boundary layer. The flow structure in the (*e*) and (*f*) sections is analysed through a simplified schematic representation and shock polar analysis. Figure 14 illustrates the schematic flow pattern beneath the Mach stem within the boundary layer. Upon entering the boundary layer, the transmitted shock ts_1 continuously bends, reflecting a series of expansion waves instead of compression waves (as shown in figure 12*e*,*f*). This behaviour contributes to the elimination of the 'shock triangle' structure following the shock intersection. Another significant observation is that the subsonic airflow is supremely superseded by fully supersonic airflow behind the transmitted shock ts_1, while the sonic line retains a shape congruent with that of the boundary layer.

The shock refraction principle between the Mach stem and the sonic line is elucidated in greater depth through the shock polar, as depicted in figure 15. The shock angle of the Mach stem, denoted as n, increases continuously, ultimately gradually transforming into a normal shock. At both ends of the Mach stem, two slip lines are pulled out, with the airflow states on either side of these slip line represented as the identical points (D_{30}–D_{50}, D_{40}–D_{60}) on the shock polar. Consequently, as one moves from D_{40} to D_{30}, the deflection angle of the airflow behind the Mach stem diminishes progressively, while the pressure experiences a minor increase. The region situated behind the Mach stem (the state between D_{30} and D_{40}) is entirely occupied by subsonic airflow, which transitions to supersonic at the lower end of the Mach stem. When the transmitted shock ts_1 penetrates the boundary layer, the reduction in incoming airflow velocity alters the angle of the transmitted shock, increasing from t_1 to t_2, t_j, until t_n, which results in a corresponding decrease in the deflection angle of the airflow. Furthermore, the decline in incoming Mach number, combined with the rise in the angle of the transmitted shock, leads to a reduction in the

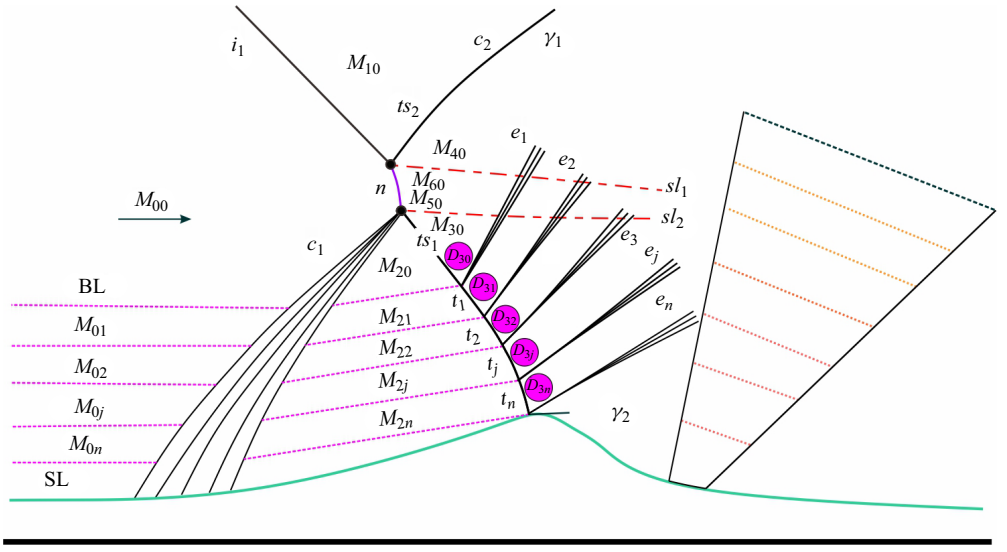

Figure 14. Refraction of the shock in the shock coalesced region: t_1, t_2, t_j, t_n, the refraction of transmitted shock in the boundary layer; D_{30}, D_{31}, D_{32}, D_{3j}, D_{3n}, the airflow parameters behind shock ts_1, t_1, t_2, t_j, t_n; sl_1, sl_2, slip line; here boundary layer BL; sonic line SL. Here $0.3 < z/D < 0.5$, Mach reflection (MR).

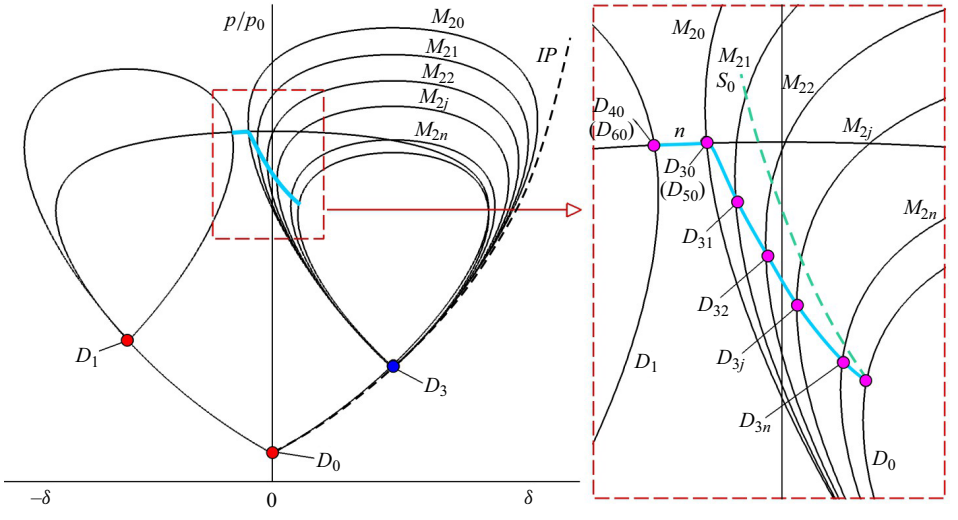

Figure 15. The expression of shock refraction in the shock-polar diagram: $0.3 < z/D < 0.5$.

Mach number downstream until the sonic line established beneath the shock t_n. The airflow following the transmitted shock migrates downward to the right-hand side, approaching the sonic line S_0, dictated by the variation trend of airflow deflection angle and Mach number. From D_{30} to D_{31}, and subsequently to D_{3j}, until D_{3n}, a series of expansion waves expand the airflow. In this intense three-dimensional flow, not only is there a modification in the near-wall separation flow, but also a fundamental transformation in the refractive phenomenon and diffraction characteristics adjacent to the boundary layer.

3.4. *Separation flow patterns near the cylinder wall*

Considering that the most prominent characteristic of the boundary layer on the cylinder, which is a curved surface with constant curvature, it is crucial for investigating the flow pattern exhibiting a three-dimensional effect on the cylinder wall. Figure 16 displays experimental and numerical oil-flow images of PSWCBLIs, where points '*S*' and '*N*' denote the saddle point and node point; red and purple dashed lines mark primary and secondary separation lines. Starting from the node point, airflow within the separation bubble deflects to the mainstream direction, then detaches from the wall at the primary separation line, and eventually reattaches to the cylinder wall at the reattachment line after a certain distance. In contrast to typical ISWBLIs on flat plates, the primary separation line of PISCBLIs exhibits a curved swept-back shape, with its curvature continuously increasing along the spanwise direction. This separation line converges into an asymptote on the leeward side of the cylinder, aligned with the mainstream direction. Furthermore, the reattachment line emitted from the nodes also exhibits a swept-back shape, bending opposite to the separation line direction. The flow field between the primary separation line and the reattachment line is intricate, showcasing a significant three-dimensional effect. Moreover, the secondary separation is generated on both sides of the cylinder wall, constituting an open-type separation observed on the wall where the airflow converges to a secondary separation line without a distinct starting edge. As this secondary separation is located on the leeward side of the cylinder, its traces are captured in the oil-flow pattern from the vertical view. In the experimental images on the left-hand side, there is an accumulation phenomenon near the primary separation line, but no significant oscillation is observed in the oil-flow streak-line patterns across the entire separation region. Even though Squire (1961) noted that oil streaks may underestimate the distance to separation, the shock-induced separated regions shown in the oil-flow visualization here remain highly reliable.

The flow patterns on the cylinder wall, captured from vertical and side views, are integrated to enhance observation and facilitate further quantitative analysis. A coordinate transformation and normalization process, expressed in the arclength formulation and azimuthal angle, was to convert flow field parameters on the cylindrical surface into a rectangular coordinate system. Figure 17 illustrates the schematic diagram of the numerical wall streamline, where surface shear stress lines are transformed based on curve length and azimuthal angle, as follows:

$$\varphi = \arcsin\left(\frac{z}{y^2 + z^2}\right), \tag{3.1}$$

$$l = \varphi\sqrt{y^2 + z^2}, \tag{3.2}$$

$$F_r = F_y \cos\varphi + F_z \sin\varphi, \tag{3.3}$$

$$F_\tau = F_z \cos\varphi - F_y \sin\varphi, \tag{3.4}$$

where y and z represent the coordinates in the vertical and spanwise directions, respectively, and l is the arclength associated with φ. Here F represents any physical vector in the three-dimensional flow field. The coordinates are converted from the x–y coordinate system to the r–τ coordinate system by introducing different vector parameters into F. The normalized flow field after the coordinate transformation is depicted in figure 17, with main flow structures marked. Red and green dots represent saddle and node points on the centreline, respectively. Purple dotted lines, purple lines and red solid lines mark the upstream influence line, primary separation line (SL_1) and the secondary separation line

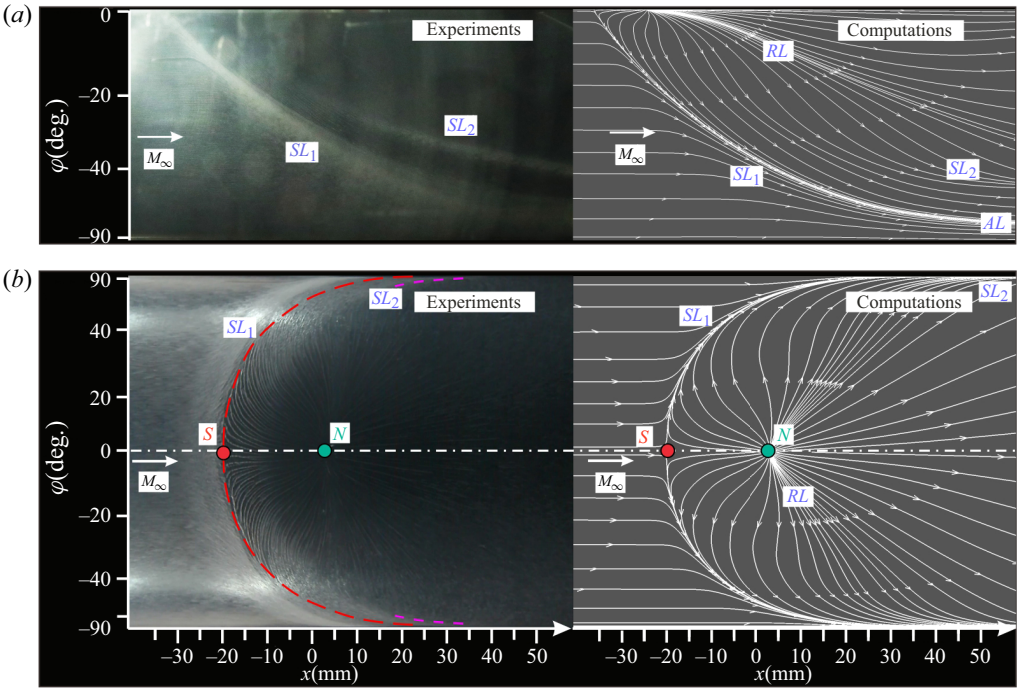

Figure 16. Experimental and numerical oil-flow patterns taken from different directions: (*a*) side view; (*b*) vertical view. Here separation line *SL*; reattachment line *RL*; asymptote line *AL*; saddle point *S*; node point *N*.

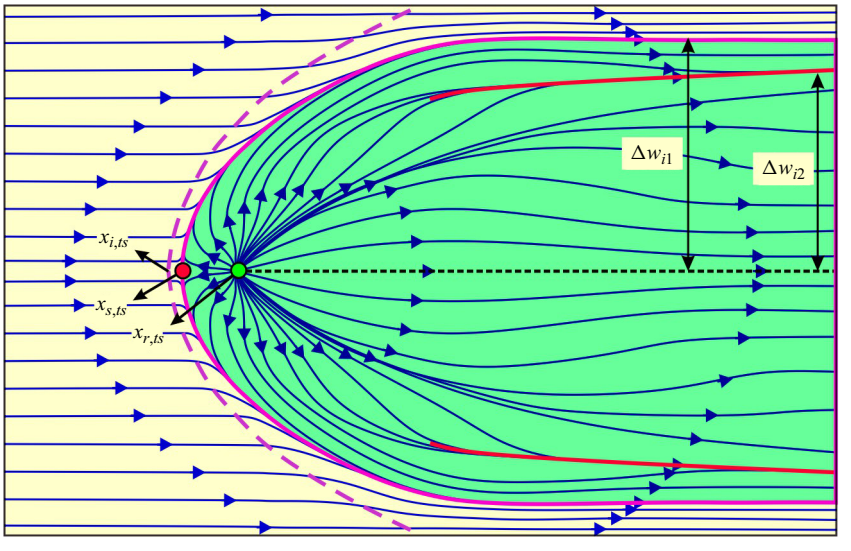

Figure 17. Schematic diagram of numerical surface streamline; cylindrical surface transformed into a rectangular plane.

	$x_{i,ts}$ (mm)	$x_{s,ts}$ (mm)	$x_{r,ts}$ (mm)	Δx_{int} (mm)	Δx_{sep} (mm)	Δw_{s_1} (mm)	Δw_{s_2} (mm)
Experimental value	−27.06	−19.96	2.58	7.54	22.54	40.25	26.65

Table 2. Transformed parameters of the flow patterns on the cylinder wall.

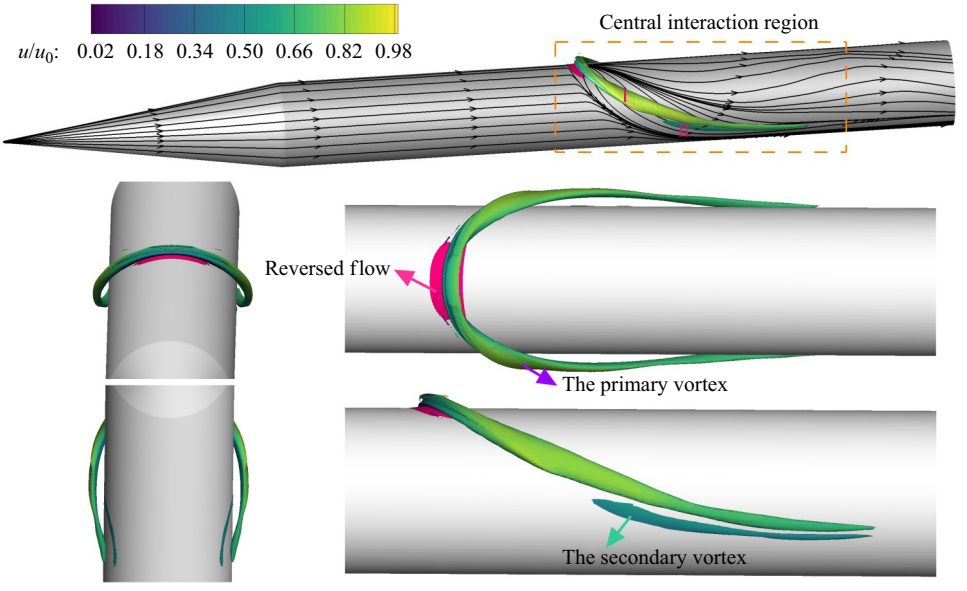

Figure 18. Vortex structure of different perspectives in the near-wall region based on Q criterion given by CFD: 1, the primary vortex; 2, the secondary vortex.

(SL_2), respectively. Meanwhile, the interaction length (Δx_{int}) is defined as the distance along the streamwise between the upstream influence line (onset of the pressure rise, $x_{s,ts}$) and the saddle point ($x_{r,ts}$), while the separation length in the centreline (Δx_{sep}) is the distance from the saddle points in the centreline ($x_{s,ts}$) to the node point ($x_{r,ts}$). The circumferential widths from the downstream positions of the primary and secondary separation lines to the centreline are designated as Δw_{s_1} and Δw_{s_2}, respectively. The transformed parameters pertinent to the separation regions are presented in table 2.

Figure 18 depicts the three-dimensional vortex structure in the near-wall region. Two counter-rotating vortices, identified using the Q-criterion, warp up around the cylinder and flow along the streamwise direction. The primary vortex experiences a significant deflection angle, approximately emanates from the initiation of the reversed flow region, where the airflow experiences a significant deflection angle, approximately 180° before colliding with the mainstream in front of the primary separation line. This vortex constantly entraining the airflow between the primary separation line and the reattachment line, while expanding in its size with a swept-back shape along the spanwise direction. As the primary vortex moves to both sides, it gradually approaches the cylinder wall, and its scale and intensity continuously decrease. The secondary flow vortex tightly adheres to the secondary separation line on the wall (figure 16). Alvi & Settles (1992) proposed that the normal Mach number $M_n = M_0 \sin \beta_0$ is the critical parameter determining the

swept shock–boundary layer interactions phenomenon, and when $1.5 < M_n < 1.9$, the lateral flow is pronounced, and secondary separation phenomenon emerges near the wall. However, in this study, the normal Mach number M_n was slightly less than 1.5, yet secondary separation was still observed near the cylinder. This finding suggests that PISCBLIs on the curved boundary layer induce more substantial lateral flow than on the flat plate, and secondary separation emerges with a smaller normal Mach number M_n.

The two separation vortices occupy the region above the primary separation line and the reattachment line and gradually dissipate along the asymptote in the downstream direction. The velocity of the fluids within the secondary vortex, as indicated in the velocity distribution legend, is markedly lower, reflecting a substantially reduced intensity compared with that of the primary vortex. The overall vortex structure generally exhibits the same swept shape as the separation line, curling along the side of the cylinder where the planar shock impinges. Previous research results (Stephen *et al.* 2013) have characterized this vortex structure as a 'concave horseshoe-shaped' cluster. Furthermore, the primary vortex exhibits significantly more prominently in scale and height than the secondary vortex. As the two vortices gradually develop downstream, they become more constrained by the cylinder wall, resulting in an alteration of their shapes and eventually evolving into a quasielliptical configuration.

3.5. *Patterns of time-mean pressure distribution on the cylinder wall*

Figure 19 presents the time-averaged static pressure distribution on the cylindrical surface at various circumferential positions ($\varphi = 0^\circ$, 20°, 60°, 100° and 180°), combining both experimental and CFD results. The red and green dotted lines in the figure represent the saddle and node points on the centreline ($\varphi = 0^\circ$), as determined in the oil-flow diagram. Notable characteristics of the separated flow within the central region of the windward side ($0^\circ < \varphi < 20^\circ$) are specifically manifested in a sharp initial increase in pressure at the interaction onset, followed by a pressure plateau. The reattachment process then occurs, exhibiting a more gradual ascent in pressure compared with the separation process. Following the attainment of the peak value at the node point, there is a progressive descending trend in pressure, attributed to the influence of the shoulder expansion fan. In the spanwise direction, the angle between the incident shock and the normal direction of the wall increases, resulting in a decreased adverse pressure gradient in the normal direction. The value of pressure plateau associated with the separation diminishes due to the intensification of lateral flow. In regions situated far from the centreline on the windward side ($60^\circ < \varphi < 180^\circ$), the peak pressure significantly decreases and the pressure plateau disappears. Furthermore, the initiation of the upstream pressure rise shifts backwards, indicating an upstream effect provoked by the swept-back pattern of the incident planar shock on the cylinder.

To elucidate the changes in the pressure plateau values mentioned previously, theoretical calculations are performed using the free interaction theory (FIT) (Chapman, Kuehn & Larson 1958), where the pressure rise during the free-interaction process is expressed as follows:

$$p/p_0 = 1 + F(\bar{x})\,\frac{\gamma}{2}M_0^2\sqrt{\frac{2C_{f,0}}{\left(M_0^2-1\right)^{0.5}}},\ \gamma = 1.4,\ \begin{cases} F(\bar{x})_{s,point} = 4.2, \\ F(\bar{x})_{s,plateau} = 6.0, \end{cases} \tag{3.5}$$

where $F(\bar{x})$ is a universal correlation function, $F(\bar{x})_{spoint}$ and $F(\bar{x})_{splateau}$ represent the values at the separation point and the separation plateau under turbulent separation, respectively. Here γ is the specific heat ratio. Based on the obtained boundary layer

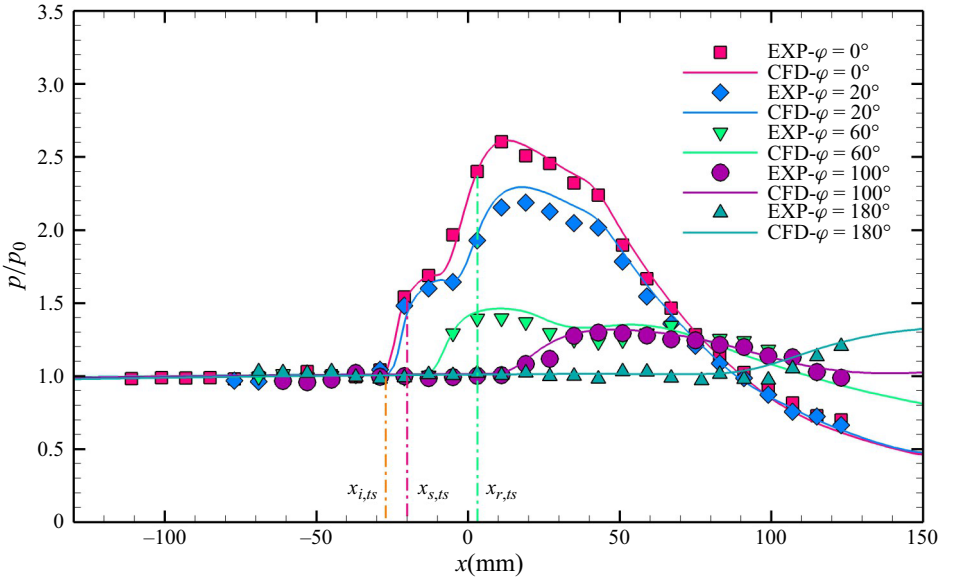

Figure 19. Comparison of time-average pressure distribution along the streamwise.

parameters of the incoming flow, the theoretical pressure rise of the separation point ($p_{t,spoint}/p_0 = 1.52$) and separation plateau ($p_{t,splateau}/p_0 = 1.74$) are obtained by substituting $C_{f,0}$ and M_0 into the relations (3.5). Moreover, the theoretical shock angle ($\alpha_s = 40.22°$) induced by separation under free interaction can be calculated by the pressure ratio relationship of the oblique shock.

The pressure ratio and separation shock angle are quantified across various spanwise sections utilizing pressure distribution measurements and schlieren imaging in both experimental and CFD analyses. The results are presented in table 3, where 'Error' denotes the relative difference between measured and theoretical values for these parameters. A comparative analysis reveals that, while the separation shock angle significantly increases along the spanwise direction, the pressure rise in the separation region (including the separation point and separation plateau) progressively decreases. This pressure change indicates that the increase in pressure rise caused by the separation shock cannot offset the decrease in pressure rise caused by lateral flow, which ultimately generates a spanwise pressure gradient. Consequently, these results lead to the release of high pressure in the separation region along with low-energy fluids. Near the symmetry plane, the interaction adheres to the FIT, as evidenced by the consistent separation shock angles and pressure increases observed on the cylindrical surface. However, as the spanwise distance increases, the measured values of separation shock angle and pressure rise show a continuously increasing difference compared with the theoretical values, signifying a gradual departure from FIT at positions on either side of the cylinder.

An analysis of the oil-flow patterns on the cylindrical surface indicates that PISCBLIs do not adhere to conical or cylindrical similarity in swept shock–boundary layer interaction. When the cylindrical surface is transformed into a rectangular plane, an elliptical configuration of the separation line of the cylindrical surface inside two side plates is unveiled. This elliptical formation bears resemblance to the intersection line of the planar incident shock on the cylinder wall. In figure 20, elliptic polar coordinates are introduced into the transformed cylindrical plane. The position of the elliptical coordinate system is

	α_s		$p_{s,point}/p_0$		$p_{s,plateau}/p_0$	
	Measured value (deg.)	Error	Measured value	Error	Measured value	Error
$z/D = 0$	39.84	−0.94 %	1.54	1.32 %	1.71	−1.72 %
$z/D = 0.1$	40.08	−0.35 %	1.42	−6.58 %	1.66	−4.59 %
$z/D = 0.2$	40.48	0.65 %	1.40	−7.89 %	1.62	−6.90 %
$z/D = 0.3$	43.96	9.30 %	1.38	−9.21 %	1.55	−10.92 %

Table 3. The measured values and relative error of the different spanwise sections; the section $z/D = 0$ represents the symmetry plane.

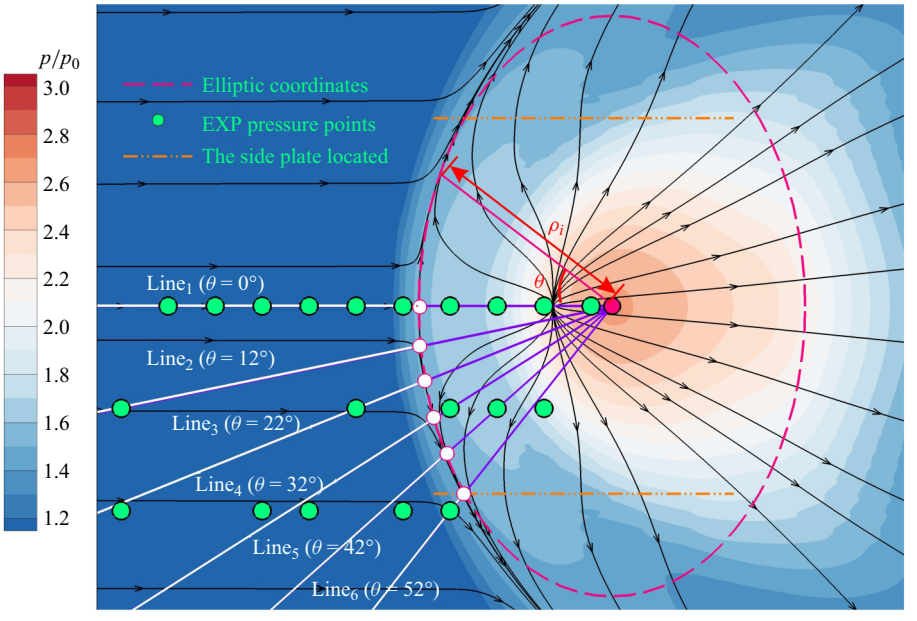

Figure 20. Schematic diagram of the establishment of the elliptic coordinate system.

established based on the separation line, where θ denotes the inclined angle between the polar axis and the x-axis, ρ symbolizes the distance between any point on the polar axis and the origin and ρ_0 represents the distance between the point on the central separation line and the origin. The centre of the ellipse is located precisely at the extremum of the pressure, from which to the upstream influence line, the pressure distribution on the cylinder wall exhibits a radial shape. Pressure on different angular polar axes is extracted from experimental and CFD results, and the dimensionless pressure distribution curve is drawn with ρ_0 as the benchmark, as shown in figure 21. Notably, it is observed that the pressure curves at different angles coincide, demonstrating a consistent pressure distribution in line with the elliptical similarity property.

This elliptical similarity fundamentally correlates with the approximate elliptical intersection line formed by the incident shock impinging on the cylindrical surface. Evidently, this elliptical similarity feature does not encompass the entirety of the separation region but is only limited to most of the reversed flow region. The primary reason for this phenomenon lies in the constrained width of the incident shock, which is limited to the region between the two side plates, allowing the incident shock to maintain

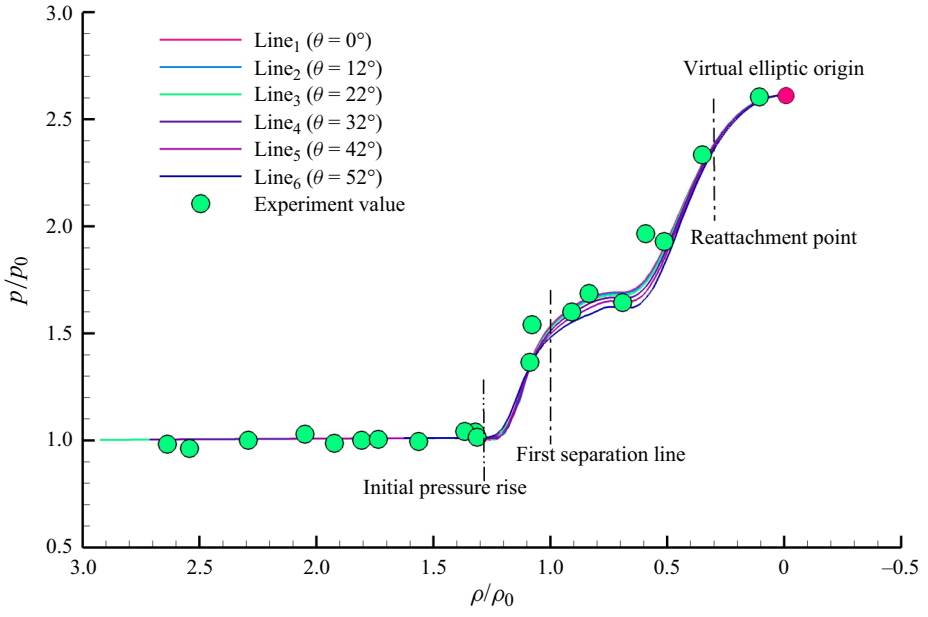

Figure 21. Pressure distribution curve on the polar axis at different angles in the elliptical coordinate system.

a planar configuration and a constant intensity. However, the incident shock sweeps back outside the side plates, resulting in a notable enhancement of the three-dimensional effects. Consequently, its strength is diminished considerably in the spanwise direction, making a huge difference in adverse pressure gradient. In the region of a large polar angle ($\theta > 50°$ or $z/D > 0.3$), the pressure distribution gradually deviates from this law. Notably, at the centre of the separation region, the lateral pressure gradient forces low-energy fluids to accumulate on both sides, resulting in a rapid decrease in pressure plateau values outside the side plates, far from the centre. This correlates with the phenomenon of pressure similarity deviating as the polar angle increases in figure 21. Therefore, the elliptical similarity criterion is only valid within the confines of the region between the side plates.

3.6. *Potential unsteady behaviour*

The time-averaged flow field characteristics of PISCBLIs are elucidated through the aforementioned schlieren images, pressure distribution and surface oil-flow topology. Notably, the separation flow induced by PISCBLIs exhibits certain unsteady behaviours, which are subsequently evaluated through various transient measurement techniques to ascertain whether these behaviours can trigger substantial alterations in the flow structure (Clemens & Narayanaswamy 2014). The low-frequency oscillation observed in the separation region is often accompanied by fluctuations in the surface pressure, therefore the dynamic pressure measurement method is utilized to capture and analyse the unsteady oscillation features within the separation region. In order to effectively capture low-frequency oscillation signals of the separation region, the measurement points of dynamic pressure are strategically positioned slightly upstream and downstream of the separation point along the centreline, with their positions indicated in figure 6.

Figure 22 presents the transient surface pressure, which clearly demonstrates a regular pattern of low-frequency oscillation. The amplitude of the pressure fluctuation signal

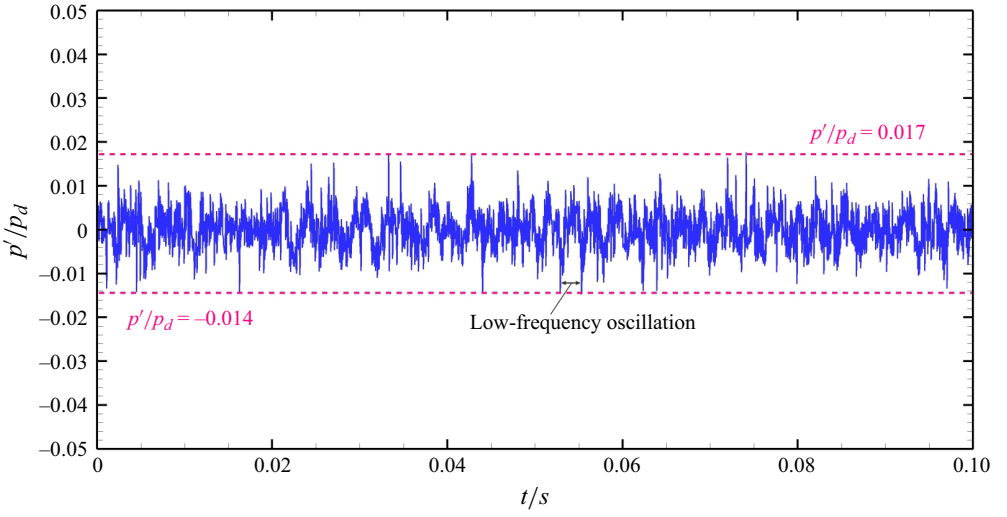

Figure 22. Pressure fluctuation signal on the wall surface.

p'/p_d $(-0.014, 0.017)$ corresponds to the oscillation range of the separation shock β'/β_2 $(-0.0086, 0.0097)$, where the p_d and β_2 represent the pressure at local measuring points and angle of separation shock, respectively. Further spectral analysis was conducted to address unsteady aspects related to separation dynamics, where the Welch method was used to calculate the power spectral density (PSD) of the pulsating pressure. As shown in figure 23, the energy of the pressure signal of both upstream boundary layer and separation bubble is mainly concentrated in the range of the low frequency, and the PSD gradually decreases with frequency. In order to better reflect the energy spectrum features of pressure fluctuation in the range of low frequency, the weighted PSD (WPSD) was obtained by the weighting of frequency. The WPSD curve of the pressure signal at the separation point reveals a pronounced peak in the low-frequency spectrum, with the characteristic frequency corresponding to the peak point determined to be 205 Hz, yielding a Strouhal number St_L of 0.0094. This Strouhal number is non-dimensionalized based on the streamwise length of the separation bubble on the centreline and the velocity of incoming flow. Clemens & Narayanaswamy (2014) discovered that in the two-dimensional SBLIs, the dimensionless characteristic frequency St_L of low-frequency oscillation is between 0.01 and 0.03. In the case of the PISCBLIs examined in this study, the Strouhal number of the low-frequency oscillation is relatively small, mainly due to the unique three-dimensional lateral flow that reduces the streamwise length of the separation region.

As shown in figure 12, figure 12(*a–c*) represent the state of the flow field in the central region, and figure 12(*e–f*) represent the state of the flow field in the two sides. Figure 12(*d*), positioned adjacent to the side plate, depicts a transitional flow field state bridging the central region and the lateral sides. In order to elucidate the effects of the impact of aforementioned low-frequency oscillation on macroscopic flow field structures and three-dimensional flow characteristics, the inviscid RR $\leftrightarrow$ MR transition criteria in the (δ_1, δ_2) plane for $Ma_0 = 2$ and $\gamma = 1.4$ is shown in figure 24. Although the separation shock angle and airflow deflection angle (δ_2) has increased in the central region (from figure 12*a* to figure 12*c*), the flow structure remains within the RR region. Conversely, as the separation shock angle continues to rise from the central area to both lateral sides (from figure 12*c* to figure 12*f*), the flow field structure enters the RR region, with the transition

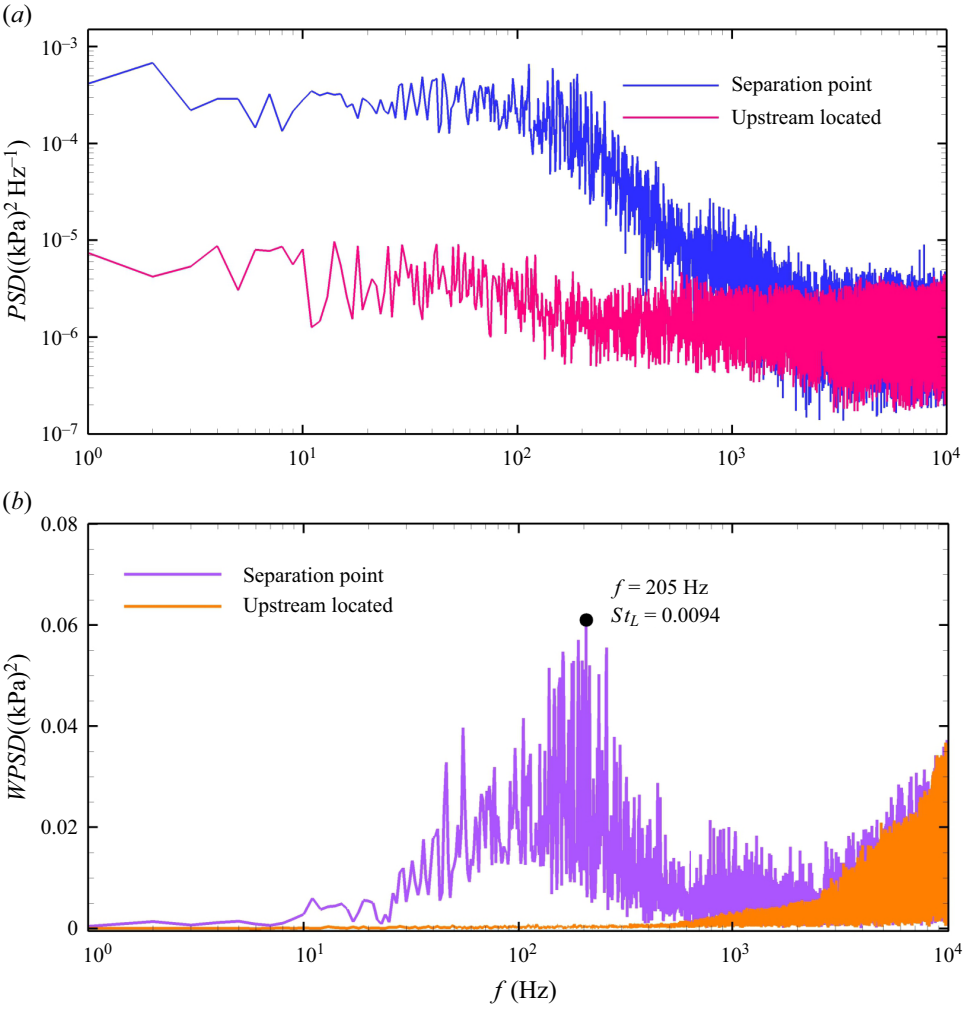

Figure 23. Fluctuating pressure signal of the upstream boundary layer and separation point: (*a*) PSD; (*b*) associated weighted PSD function.

location occurring outside of the side plate. The analysis reveals that the fluctuations caused by the PISCBLIs itself or the low-frequency oscillations are insufficient to initiate the transition from RR to MR for the considered flow conditions. As low-energy fluid accumulates towards both sides due to the lateral flow effect, an increase in the angle of the compression wave induced the flow to completely transform into MR. Similarly, the low-frequency oscillations here are insufficient strong to return to the RR. Hence, the RR ↔ MR transition predominantly driven by the increase in the angle of separation shock (or compression wave), rather than through unsteady disturbance. In figure 12(*d*), characterized as transitional and situated near the side plate, the flow exhibits considerable complexity, displaying unsteady behaviours that engender mutual transformations between RR and MR. Note that these interactions occur primarily on a microscopic scale.

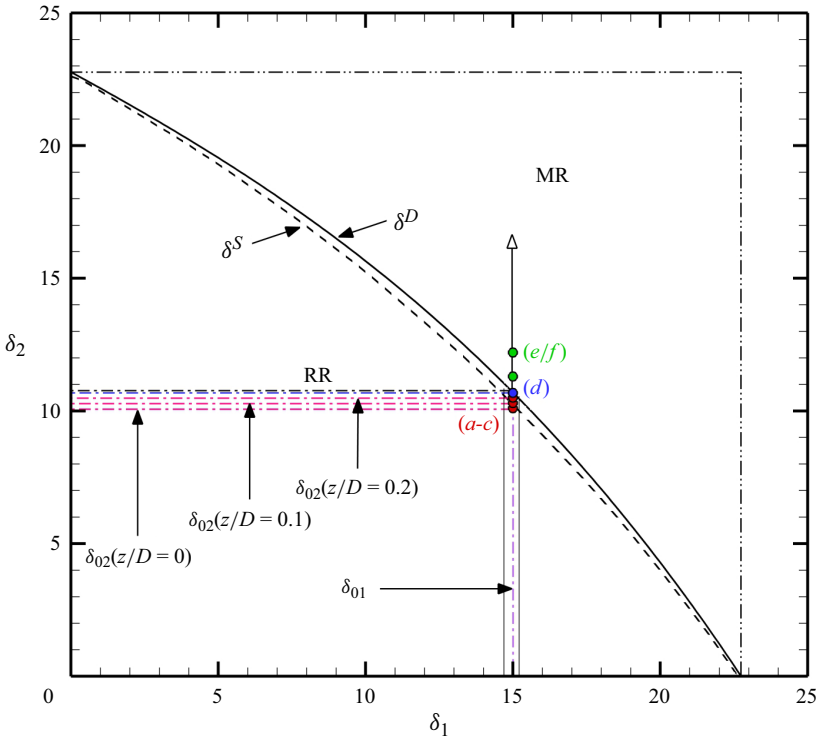

Figure 24. Analytical results for the RR ↔ MR transition criteria in the (δ_1, δ_2) plane for $Ma_0 = 2$ and $\gamma = 1.4$: (*a*) $z/D = 0$; (*b*) $z/D = 0.1$; (*c*) $z/D = 0.2$; (*d*) $z/D = 0.3$; (*e*) $z/D = 0.4$; (*f*) $z/D = 0.45$. Sonic (δ^S) criteria as proposed by Hu *et al.* (2009); detachment (δ^D) as proposed by Li, Chpoun & Ben-dor (1999) for asymmetric shock intersections.

4. Conclusions

This study investigates the interaction between the planar shock with finite width and a cylindrical boundary layer under Mach 2.0 flow through wind-tunnel experiments, CFD methods and theoretical analysis. The three-dimensional flow characteristics of PISCBLIs are captured and quantified using schlieren photography, pressure measurement and oil-flow visualization. Moreover, potential unsteady behaviours of the separated flow are analysed and evaluated through transient pressure signals and flow visualization.

The results indicate that the planar shock impinging on the cylinder wall leads to a distinct bending shape within the boundary layer, deviating from the quasi-two-dimensional property. In the vicinity of the symmetry plane, a transmitted shock ts_1 refracts within the boundary layer, bending in the outer boundary layer and reflecting a series of compression waves to coalesce a 'shock triangle' with the transmitted shock ts_1 and ts_2. This triangular scale continuously diminishes until it vanishes at the edge of the generator, progressing along the spanwise direction. Outside the side plate, the planar shock degenerates into a swept shock, sweeping back along the spanwise direction. The initial 'shock triangle' structure gives way to a Mach stem, with refracted compression waves transformed into expansion waves. Airflow diffusion increases the separation region height along the streamwise direction, slightly raising the separation shock angle and inducing Mach stem generation with widening spanwise width.

Significant changes in the circumferential direction of the wall surface have been observed. Oil-flow visualization methods depict the flow patterns on the cylindrical

wall from both vertical and lateral perspectives, providing a comprehensive view of the PICSBLIs. The flow topology on the cylindrical surface comprises a saddle point, a node point, two separation lines and a reattachment line. The primary separation line, originating from the centreline, demonstrates a swept-back configuration that ultimately converges towards an asymptote. In contrast, the secondary separation line, positioned farther downstream, develops in tandem with the primary separation line, correlating with the emergence of the Mach stem. Above the primary separation line, two strands of symmetrical and swept horseshoe vortices are generated, exhibiting opposite directions of rotation and varying scales. These vortices ultimately wrap around the cylindrical surface and gradually deflect towards a direction aligned with the mainstream flow.

As the separation region diffuses in the circumferential direction of the cylinder, the initial pressure rise and separation shock angle in the symmetry plane still conform to the principles of FIT. However, in the peripheral regions, due to the accumulation effect of low-energy fluids, the separation shock angle significantly increases, accompanied by a reduction in the pressure on the separation platform. The pressure distribution along the wall reveals an elliptical similarity property. The centre of the elliptical distribution coincides precisely with the peak pressure point. This elliptical similarity property illustrates a transition from a flat plate to a cylinder surface based on the shape and curvature of the separation line, showcasing the distinctive characteristic of the curved boundary layer on a cylinder wall.

Furthermore, the separation flow induced by PISCBLIs exhibits certain low-frequency oscillation phenomenon, with the feature frequency corresponding to the peak point measured at 205 Hz and a Strouhal number St_L of 0.0094. Nevertheless, this potential unsteady behaviour observed is insufficient to trigger substantial alterations in the mean flow field structure.

Acknowledgements. This work is performed at the High Performance Computing Platform of Nanjing University of Aeronautics and Astronautics. The authors are grateful to the editor and the reviewers for their valuable work in improving the quality of the paper.

Funding. This work is funded by the National Natural Science Foundation of China (grant nos 12272177, 12025202 and U20A2070), National Science and Technology Major Project (J2019-II-0014-0035), Young talent lift project (2021-JCJQ-QT-064) and Project from Advanced Jet Propulsion Innovation Center, AEAC (project ID. HKCX202-02-005).

Declaration of interests. The authors report no conflict of interest.

Author ORCIDs.
Fangbo Li https://orcid.org/0009-0005-9666-8607;
Hexia Huang https://orcid.org/0000-0001-5193-6384;
Huijun Tan https://orcid.org/0000-0002-5093-7278;
Xin Li https://orcid.org/0000-0002-8854-3733;
Yuan Qin https://orcid.org/0009-0002-0487-2423.

Appendix

Due to the limited information obtained from the experimental study, it is difficult to present a complete three-dimensional flow field structure and vortex features. Therefore, CFD methods are introduced to verify the experimental results and supplement three-dimensional flow characteristics. To ensure the rationality and accuracy of CFD results, specific verification undoubtedly needs to be carried out based on the simulation calculation methods before applying it. In response to the interaction phenomenon induced

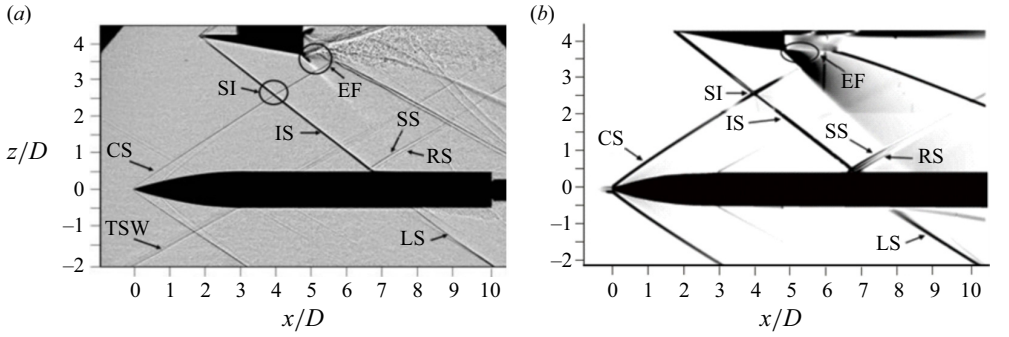

Figure 25. Comparison of flow field structures between the CFD and experiment: (*a*) experiment result; (*b*) CFD result. Shock-shock intersection (SI), expansion fan (EF), conical shock (CS), incident shock (IS), separation shock (SS), reattachment shock (RS), test section Mach wave (TSW), leeward shock (LS).

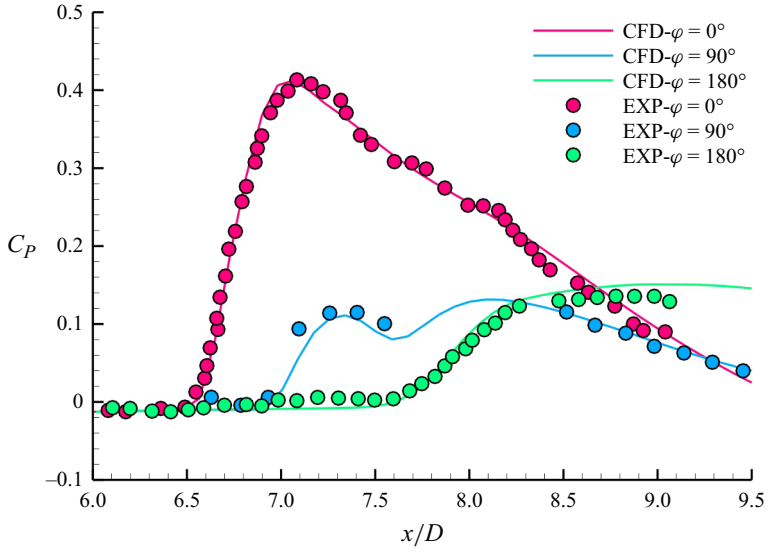

Figure 26. Comparison of streamwise pressure at different circumferential positions.

by two-dimensional shocks incident on the cylindrical boundary layer, the CFD method was used to numerically calculate the experimental results of Mason *et al.* (2021). Due to the large density gradient around the shock, the grid density cannot meet the requirements for reproducing the refined flow field. Therefore, adaptive grid refinement technology was used to iterate the calculation results several times. The specific grid partitioning method and boundary conditions have been provided earlier, which remain completely consistent here.

The verification results indicate that the flow field structure obtained by CFD methods is almost identical to the experimental results. As shown in figure 25, except for the presence of wind tunnel clutter in the test results, the other wave system structures were accurately reproduced, and the separation shock and reattachment shock angles were basically consistent with the experimental results. Comparing the pressure distribution along the streamwise direction between CFD and experimental results, as shown in figure 26, the dimensionless pressure C_p of CFD and experimental results demonstrate good consistency

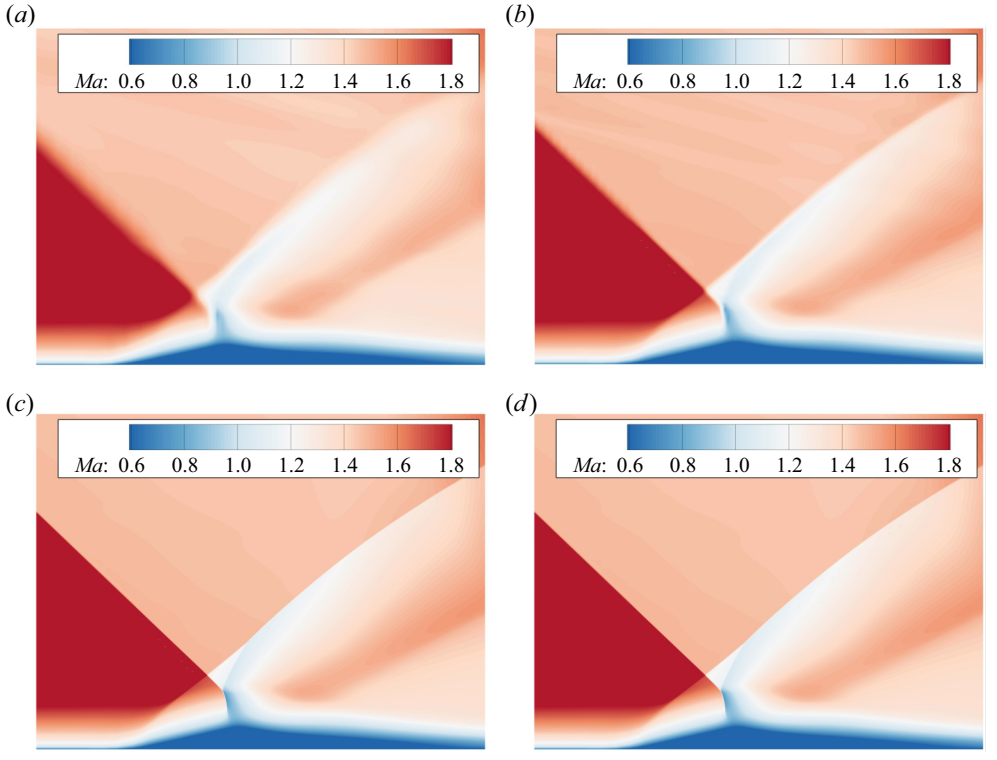

Figure 27. The flow field structure in the symmetry plane under different grid resolutions: (*a*) 8×10^6 grids; (*b*) 12×10^6 grids; (*c*) 16×10^6 grids; (*d*) 20×10^6 grids.

at different positions in the circumferential direction. The onset position and peak value of the pressure rise are well matched. The consistency between the schlieren image and pressure results provides high credibility and accuracy for the CFD method, especially in the presence of separation induced by SWBLIs. Therefore, the CFD methods used in this study have capable credibility and reliability in the research of PISCBLIs.

In order to demonstrate the accuracy and rationality of the grid resolution used in this manuscript, several grid resolutions with difference degrees of freedom are conducted for numerical calculations on the PISCBLIs, while the grid structure does not undergo any changes. The initial grid resolution is 8×10^6 degrees of freedom, and then adaptive grid technology is used to refine it for many times. Three grid computational domains with grid resolutions of 12×10^6, 16×10^6 and 20×10^6 degrees of freedom are generated through these iterations. The numerical simulations are conducted on these four different grid resolutions.

Figure 27 compares the flow field structures in the symmetry plane of these four grid resolutions, and it is found that the adaptive refinement of the grid does not change the flow field structure. The main flow features with 8×10^6 and 12×10^6 grids are not clear, while the shock triangle structure and separated flow are accurately captured as the grid resolution reaches 16×10^6. Over 16×10^6 degrees of grids, the flow field structures do not further manifest significant changes with the increasing of the grid resolution. The same conclusion is also obtained from the wall pressure curves, as shown in figure 28. The wall pressure of lower grid resolution deviates by that of more than the grid resolutions more than 16×10^6 within the separation region and after pressure peak, while the latter

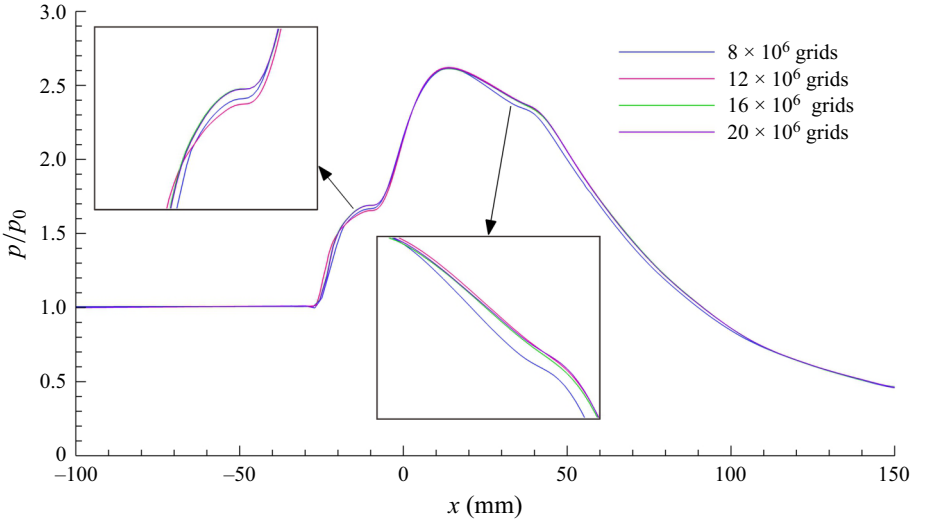

Figure 28. Comparison of wall pressure distribution under different grid resolutions.

remain consistent overall. Considering both the accuracy of simulation and the saving of computational resources, the grid of 16×10^6 is considered an appropriate and accurate grid resolution, and the numerical simulations in this manuscript all rely on this grid resolution.

References

ALVI, F.S. & SETTLES, G.S. 1992 Physical model of the swept shock wave/boundary-layer interaction flowfield. *AIAA J.* **30** (9), 2252–2258.

ANDERSON, J.D. 2010 *Fundamentals of Aerodynamics*. McGraw-Hill Education.

BABINSKY, H. & HARVEY, J.K. 2011 *Shock Wave-Boundary-Layer Interactions*. Cambridge University Press.

BABINSKY, H. & OGAWA, H. 2008 SBLI control for wings and inlets. *Shock Waves* **18** (2), 89–96.

BARRY, F.W., SHAPIRO, A.H. & NEUMANN, E.P. 1951 Numerical study on wall temperature effects on shock wave/turbulent boundary-layer interaction. *J. Aeronaut. Sci.* **18** (4), 229–238.

BHARDWAJ, S., HEMANTH CHANDRA VAMSI, K. & SRIRAM, R. 2022 On the scaling of three-dimensional shock-induced separated flow due to protuberances. *Phys. Fluids* **34** (7), 076115.

BROSH, A., KUSSOY, M.I. & HUNG, C.M. 1985 Experimental and numerical investigation of a shock wave impingementon a cylinder. *AIAA J.* **23** (6), 840–846.

CHANG, J.T., LI, N., XU, K.J., BAO, W. & YU, D.R. 2017 Recent research progress on unstart mechanism, detection and control of hypersonic inlet. *Prog. Aeosp. Sci.* **89**, 1–22.

CHAPMAN, D.R., KUEHN, D.M. & LARSON, H.K. 1958 Investigation of separated flows in supersonic and subsonic streams with emphasis on the effect of transition. *NACA Tech. Rep.* NACA-TR-1356.

CLEMENS, N.T. & NARAYANASWAMY, V. 2014 Low-frequency unsteadiness of shock wave/turbulent boundary layer interactions. *Annu. Rev. Fluid Mech.* **46** (1), 469–492.

COMBS, C.S., LASH, E.L., KRETH, P.A. & SCHMISSEUR, J.D. 2018 Investigating unsteady dynamics of cylinder-induced shock-wave/transitional boundary-layer interactions. *AIAA J.* **56** (4), 1588–1599.

DÉLERY, J. 1985 Shock wave/turbulent boundary layer interaction and its control. *Prog. Aeosp. Sci.* **22**, 209–280.

DÉLERY, J. 1993 Contribution of laser doppler velocimetry to the physical description of shock wave/turbulent boundary layer interaction with incidence on turbulence modeling. *Tech. Rep.* 792. AGARD/FDP-VKI Special Course on Shock Wave B̃oundary Layer Interactions in Supersonic and Hypersonic Flows.

DÉLERY, J. & MARVIN, J.G. 1986 Shock-wave boundary layer interactions. *Tech. Rep.* 280. AGARDograph.

DOLLING, D.S. 2001 Fifty years of shock-wave/boundary-layer interaction research: what next? *AIAA J.* **39** (8), 1517–1531.

VAN DRIEST, E.R. 1951 Turbulent boundary layer in compressible fluids. *J. Aeronaut. Sci.* **18** (3), 145–160.

DUPONT, P., HADDAD, C. & DEBIÈVE, J.F. 2006 Space and time organization in a shock-induced separated boundary layer. *J. Fluid Mech.* **559**, 255–277.

FAGE, A. & SARGENT, R.H. 1947 Shock-wave and boundary-layer phenomena near a flat surface. In *Proceedings of the Royal Society of London*, vol. 190, pp. 1–20. Royal Society of London.

FANG, J., ZHELTOVODOV, A.A., YAO, Y., MOULINEC, C. & EMERSON, D.R. 2020 Comparative study on single-incident and 1 dual-incident shock wave / turbulent boundary layer 2 interactions with identical total deflection angle. *J. Fluid Mech.* **940** (A7), 1–37.

FERRI, A. 1940 Experimental results with airfoils tested in the high-speed tunnel at Guidonia. *NACA Tech. Mem.* NACA-TM-946.

GAI, S.L. & TEH, S.L. 2000 Interaction between a conical shock wave and a plane turbulent boundary layer. *AIAA J.* **38** (5), 804–811.

GAITONDE, D.V. 2015 Progress in shock wave/boundary layer interactions. *Prog. Aeosp. Sci.* **72**, 80–99.

GAITONDE, D. & KNIGHT, D. 1991 Numerical investigation of bleed on three-dimensional turbulent interactions due to sharp fins. *AIAA J.* **29** (11), 1878–1885.

GARCIA, M., HOFFMAN, E.N.A., LALONDE, E.J., COMBS, C.S., POHLMAN, M., SMITH, C., GRAGSTON, M.T. & SCHMISSEUR, J.D. 2018 Effects of surface roughness on shock-wave/turbulent boundary-layer interaction at mach 4 over a hollow cylinder flare model. *Fluids* **7** (9), 286.

GREEN, J.E. 1970 Interactions between shock waves and turbulent boundary layers. *Prog. Aeosp. Sci.* **11**, 235–340.

GROSSMAN, I.J. & BRUCE, P.J.K. 2018 Confinement effects on regular–irregular transition in shock-wave–boundary-layer interactions. *J. Fluid Mech.* **853**, 171–204.

HENDERSON, L.F. 1966 The refraction of a plane shock wave at a gas interface. *J. Fluid Mech.* **26**, 607–637.

HENDERSON, L.F. 1967 The reflexion of a shock wave at a rigid wall in the presence of a boundary layer. *J. Fluid Mech.* **30**, 699–722.

HERRMANN, C. & KOSCHEL, W. 2002 Experimental investigation of the internal compression inside a hypersonic intake. *AIAA Paper* 2002-4130.

HU, Z.M., MYONG, R.S, KIMAND, M.S. & CHO, T.H. 2009 Downstream flow condition effects on the rr $\rightarrow$ mr transition of asymmetric shock waves in steady flows. *J. Fluid Mech.* **620**, 43–62.

HUANG, H.X., *et al.* 2023 A review of the shock-dominated flow in a hypersonic inlet/isolator. *Prog. Aeosp. Sci.* **143**, 376–421.

HUANG, H.X., TAN, H.J., SUN, S. & WANG, Z.Y. 2018 behavior of shock train in curved isolators with complex background waves. *AIAA J.* **56** (1), 329–341.

KENDALL, A. & KOOCHESFAHANI, M. 2008 A method for estimating wall friction in turbulent wall-bounded flows. *Exp. Fluids* **44** (5), 773–780.

KIRIAKOS, R.M., POURNADALI KHAMSEH, A., GIANOUKAKIS, G. & DEMAURO, E.P. 2022 PIV investigation of the effects of shock generator wedge angle and trailing-edge expansion waves on impinging shock/turbulent boundary layer interactions over a cylinder. *AIAA Paper* 2022-1328.

KRISHNAN, L., SANDHAM, N.D. & STEELANT, J. 2009 Shock-wave/boundary-layer interactions in a model scramjet intake. *AIAA J.* **47** (7), 1680–1691.

KUBOTA, H. & STOLLERY, J.L. 1982 An experimental study of the interaction between a glancing shock wave and a turbulent boundary layer. *J. Fluid Mech.* **116**, 431–458.

KUMAR, P. & MAHESH, K. 2018 Analysis of axisymmetric boundary layers. *J. Fluid Mech.* **849**, 927–941.

KUSSOY, M.I., VIEGAS, J.R. & HORSTMAN, C.C. 1980 Investigation of a three-dimensional shock wave separated turbulent boundary layer. *AIAA J.* **18** (12), 1477–1484.

LI, H., CHPOUN, A. & BEN-DOR, G. 1999 Analytical and experimental investigations of the reflection of asymmetric shock waves in steady flows. *J. Fluid Mech.* **390**, 25–43.

LI, X., ZHANG, Y., TAN, H.J., JIN, Y. & LI, C. 2022 Comparative study on single-incident and 1 dual-incident shock wave / turbulent boundary layer 2 interactions with identical total deflection angle. *J. Fluid Mech.* **940** (A7), 1–34.

LI, X., ZHANG, Y., TAN, H.J., SUN, S., YU, H. & JIN, Y. 2023 Separation length scaling for dual-incident shock 1 wave/turbulent boundary layer interactions with 2 different shock wave distances. *J. Fluid Mech.* **940** (A7), 1–34.

LIEPMANN, H.W., ROSHKO, A. & DHAWAN, S. 1952 *On Reflection of Shock Waves from Boundary Layers*. *NACA Tech. Rep.* NACA-TR-1100.

LINDÖRFER, S.A., COMBS, C.S., KRETH, P.A., BOND, R.B. & SCHMISSEUR, J.D. 2020 Scaling of cylinder-generated shock-wave/turbulent boundary-layer interactions. *Shock Waves* **30** (4), 395–407.

LUEPTOW, R.M. 1990 Turbulent boundary layer on a cylinder in axial flow. *AIAA J.* **28** (10), 1705–1706.

MASON, F., NATARAJAN, K. & KUMAR, R. 2021 Shock-wave/boundary-layer interactions on an axisymmetric body at Mach 2. *AIAA J.* **59** (11), 4530–4543.

MONKEWITZ, P.A. & NAGIB, H.M. 2023 The hunt for the Kármán 'constant' revisited. *J. Fluid Mech.* **967** (A15), 1–19.

MORKOVIN, M.V., MIGOTSKY, E., BAILEY, H.E. & PHINNEY, R.E. 1952 Experiments on interaction of shock waves and cylindrical bodies at supersonic speeds. *J. Aeronaut. Sci.* **19** (4), 237–248.

NIMURA, K., TSUTSUI, F., KTAMURA, K. & NONAKA, S. 2023 Aerodynamic effects of surface protuberance sizes on slender-bodied supersonic vehicle. *AIAA Paper* 2023-0241.

NOMPELIS, I., CANDLER, G.V. & HOLDEN, M.S. 2003 Effect of vibrational nonequilibrium on hypersonic double-cone experiments. *AIAA J.* **41** (11), 2162–2169.

PANARAS, A.G. 1996 Review of the physics of swept-shock/boundary layer interactions. *Prog. Aeosp. Sci.* **32**, 173–244.

PANOV, Y.A. 1971 Interaction of incident three-dimensional shock with a turbulent boundary layer. *Fluid Dyn.* **3** (3), 108–110.

PICKLES, J.D., METTU, B.R., SUBBAREDDY, P.K. & NARAYANASWAMY, V. 2019 On the mean structure of sharp-fin-induced shock wave/turbulent boundary layer interactions over a cylindrical surface. *J. Fluid Mech.* **865**, 212–246.

RAMESH, M.D. & TANNEHILL, J.C. 2004 Correlations to predict the streamwise influence regions in supersonic turbulent flows. *J. Aircraft* **41** (2), 274–283.

ROBERTSON, G., KUMAR, R., EYMANN, A.T. & MORTON, S.A. 2015 Experimental and numerical study of shock-wave boundary layer interactions on an axisymmetric body. *AIAA Paper* 2015-2935.

SABNIS, K. & BABINSKY, H. 2023 A review of three-dimensional shock wave–boundary-layer interactions. *Prog. Aeosp. Sci.* **89**, 1–22.

SCHMISSEUR, J.D. & DOLLING, D.S. 1994 Fluctuating wall pressures near separation in highly swept turbulent interactions. *AIAA J.* **32** (6), 1151–1157.

SEDNEY, R. 1973 A survey of the effects of small protuberances on boundary-layer flows. *AIAA J.* **11** (6), 782–792.

SETTLES, G.S. & KIMMEL, R.L. 1986 Similarity of quasi conical shock wave/turbulent boundary-layer interactions. *AIAA J.* **24** (1), 47–53.

SETTLES, G.S. & LU, F.K. 1985 Conical similarity of shock/boundary-layer interactions generated byswept and unswept fins. *AIAA J.* **23** (7), 1021–1027.

SHENG, F.J., TAN, H.J., ZHUANG, Y., HUANG, H.X., CHEN, H. & WANG, W.X. 2018 Visualization of conical vortex and shock in swept shock/turbulent boundary layer interaction flow. *J. Vis.* **21** (6), 909–914.

SHUTTS, W.H., HARTWIG, W.H. & WEILER, J.E. 1955 Final report on turbulent boundary layer and skin friction measurements on a smooth, thermally insulated flat plate at supersonic speeds. *Tech. Rep.* Defence Research Laboratory, the University of Texas.

SOUVEREIN, L.J., BAKKER, P.G. & DUPONT, P. 2013 A scaling analysis for turbulen shock-wave/boundary-layer interactions. *J. Fluid Mech.* **714**, 505–535.

SQUIRE, L.C. 1961 The motion of a thin oil sheet under the steady boundary layer on a body. *J. Fluid Mech.* **11** (2), 167–179.

SRIRAM, R., SRINATH, L., DEVARAJ, M.K.K. & JAGADEESH, G. 2016 On the length scales of hypersonic shock-induced large separation bubbles near leading edges. *J. Fluid Mech.* **806**, 304–355.

STEPHEN, E.J., FARNSWORTH, J.A., PORTER, C.O., DECKER, R., MCLAUGHLIN, T.E. & DUDLEY, J.G. 2013 Impinging shock-wave boundary-layer interactions on a three-dimensional body. *AIAA Paper* 2013-2733.

VOITENKO, D.M., ZUBKOV, A.I. & PANOV, Y.A. 1966 Supersonic gas flow past a cylindrical obstacle on a plate. *Fluid Dyn.* **1** (1), 84–88.

VOLPIANI, P.S., BERNARDINI, M. & LARSSON, J. 2018 Effects of a nonadiabatic wall on supersonic shock/boundary-layer interactions. *Phys. Rev. Fluids* **3** (8), 083401.

WHITE, F.M. & MAJDALANI, J. 2006 *Viscous Fluid Flow*. McGraw-Hill Education.

WRIGHT, M.J., SINHA, K., OLEJNICZAK, J., CANDLER, G.V., MAGRUDER, T.D. & SMITS, A.J. 2000 Numerical and experimental investigation of double-cone shock interactions. *AIAA J.* **38** (12), 2268–2276.

ZHU, X.K., YU, C.P., TONG, F.L. & LI, X.L. 2017 Numerical study on wall temperature effects on shock wave/turbulent boundary-layer interaction. *AIAA J.* **55** (1), 131–140.

ZUO, F.Y., MEMMOLO, A., HUANG, G.P. & PIROZZOLI, S. 2019 Direct numerical simulation of conical shock wave–turbulent boundary layer interaction. *J. Fluid Mech.* **877**, 167–195.